GALAXY EVOLUTION IN GROUPS AND CLUSTERS WITH ILLUSTRISTNG

THE EVOLUTION OF GALAXY STAR FORMATION AND MORPHOLOGY IN GROUPS AND CLUSTERS WITH ILLUSTRISTNG

By JING YEUNG, BSs

A Thesis Submitted to the School of Graduate Studies in Partial Fulfillment of the Requirements for the Degree Master of Science

McMaster University

MASTER OF SCIENCE (2025)

Hamilton, Ontario, Canada (Physics and Astronomy)

TITLE:	The Evolution of Galaxy Star Formation and Morphology in Groups and Clusters with IllustrisTNG
AUTHOR:	Jing Yeung BSs (Physics and Astronomy), University of Manitoba, Winnipeg, Canada
SUPERVISOR:	Laura Parker
NUMBER OF PAGES:	xi, 98

Abstract

Galaxies residing in groups and clusters have long been observed to show lower star formation rates and a higher fraction of early-type morphologies compared to field populations, highlighting the significant role of environment effects in galaxy evolution. Recent observational studies indicate that the fractions of bulge-dominated and quenched galaxies increase with time since infall into dense environments. However, due to projection effects, the timescales and dominant mechanisms driving these changes remain under debate. This thesis investigates how galaxy star formation and morphology evolve following infall into groups and clusters, using the state-of-the-art hydrodynamical simulation IllustrisTNG100-1. We find that the star formation and morphology of TNG100 satellites change as a function of infall time in a way similar to low-z observations, but low-mass satellites in TNG100 are systematically more quenched than observed galaxies. Moreover, satellites tend to quench and build up their bulges more rapidly than central galaxies, following a two-stage evolutionary scenario in which star formation is suppressed prior to major structural changes.

Acknowledgments

It has been such an honour to be part of the Astronomy and Physics family at McMaster over the past two years. The support, encouragement, and friendships I have found here have made this experience truly special.

First, I want to thank my supervisor, Dr. Laura Parker, for all the patience, guidance, and encouragement throughout this journey, ensuring that I stayed on track. I am truly grateful for the opportunities and insights you have provided, and for the support and mentorship you have given me over these two years. I also want to thank my undergraduate supervisor, Dr. Jayanne English, for introducing me into the world of galaxy evolution and for all the help and advice that continued well beyond my undergraduate years.

To my group members—Megan, Lauren, Dylan, and Matías—thank you for all the help, feedback, and jokes. You made research so much easier and a lot more fun. To my friends at McMaster, thank you for filling my life here with joy and memories I will never forget. A special shoutout to Billy for organizing squash and being such a great host when I visited Calgary. Raven, Kait, Ran, Dhruval, and Jinoo, thank you for all the small moments and coffee breaks that made my life here so much more enjoyable. To my office mates, thanks for the laughs, random chats, and for making the office a place I actually looked forward to being in.

To my friends back in Hong Kong—Mung Shan, the "Changers", Bobby, and Jasmine—thank you for all the fun times, the laughs, and the moments that made even the distance feel shorter. I have known all of you for more than ten years, and your friendship has meant so much. A special thank you to Mung Shan for all the years we have spent together, from preparing for our high-school public exams to staying in touch and supporting each other even after I moved to Canada.

A big thank you to my mom and dad, as well as everyone in the family, for always supporting me and being patient with me, no matter what.

Finally, I want to thank Vivian. Through every exam period, deadline, and stressful moment, you were always there to support me and cheer me up. You made me smile when I needed it most, and you never hesitated to give up your weekends just to sit beside me while I studied. Those moments meant more than I can put into words. Thank you for walking with me through this journey—I truly could not have done it without you.

Table of Contents

List of Figures

List of Tables

Chapter 1

Introduction

For thousands of years, people across cultures have observed the night sky, tracking the motion of stars and planets. Among the pinpoint-like stars, ancient observers also noticed fuzzy, diffuse objects—now known as deep sky objects. Some, like the star cluster Pleiades (the Seven Sisters), are objects within the Milky Way. Others, including the Andromeda Galaxy, were long debated until the early 20th century, when Edwin Hubble provided definitive evidence that Andromeda lies far beyond our galaxy (Hubble, 1929). This discovery marked the beginning of our understanding that the Milky Way is just one of many galaxies in the Universe. Since then, technological advancements have vastly expanded our knowledge of galaxy formation and evolution.

We now know that the Universe contains billions of galaxies, exhibiting a wide variety of properties, including differences in mass, morphology, colour, and star formation activity. In this chapter, I provide an overview of galaxy properties, the characteristics of the environments in which galaxies reside, and a summary of the processes that drive their evolution over cosmic time.

1.1 Galaxy Properties

1.1.1 Components and Structure of Milky Way-like Galaxies

Galaxies are collections of stars, multi-phase gas, dust, and dark matter. Our Galaxy, the Milky Way, belongs to the class of disk galaxies. These systems are characterized by a dense central region, extended stellar and gaseous components, all embedded within a massive dark matter halo. These components, ordered roughly from most to least centrally concentrated, together shape a galaxy's morphology, dynamics, and evolution. Their relative prominence varies depending on a galaxy's morphological type (Section 1.1.2) and its surrounding environment (Section 4.4). The structure of Milky Way-like galaxies generally includes:

- Bulge: The dense, spheroidal central region dominated by an old stellar population with largely random motions.
- Stellar disk: A flattened, rotationally supported structure containing young and intermediate-age stars, along with dust.
- Gas disk: An extended disk rich in cold atomic (HI) and molecular (H_2) gas, which serves as the primary fuel for star formation.
- Circumgalactic medium (CGM): A diffuse halo of hot, ionized gas that surrounds the galaxy. It acts as a reservoir that can replenish the gas disk through accretion.
- Dark matter halo: The dominant mass component that governs the galaxy's gravitational potential.

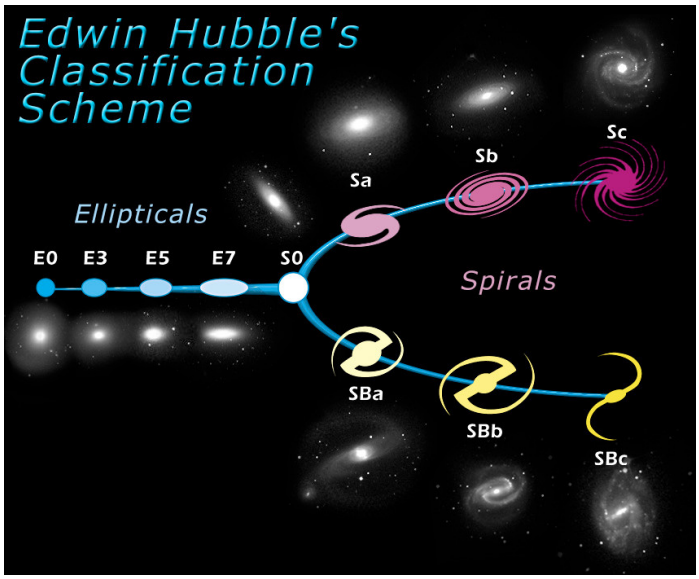

Figure 1.1: The Hubble tuning fork is a classification scheme for galaxies based on their visual appearance. Ellipticals and spirals are on the left and right, respectively. Hubble originally believed that galaxies evolved from ellipticals to spirals, hence the terms "early-type" and "late-type" (e.g. Carroll & Ostlie, 2017). Image credit: NASA & ESA

1.1.2 Morphology

Visual Morphology

Edwin Hubble's classification system (Hubble, 1926) marked the first structured attempt to categorize galaxy morphology, introducing three principal types: elliptical, spiral, and irregular, now known as the Hubble Tuning Fork (Figure 1.1). Elliptical galaxies are smooth and featureless, ranging from nearly spherical shapes (E0) to highly elongated (E7). Spiral galaxies, by contrast, feature a central bulge and well-defined spiral arms, and are further classified based on the presence/absence of a central bar, as well as the size of the bulge relative to the disk. Later updates to Hubble's system introduced lenticular (S0) galaxies, which display a bulge–disk structure without spiral arms and are considered transitional between ellipticals and

spirals. It is common to refer to elliptical and S0 galaxies as early-type, and all spiral types as late-type. Galaxies that do not fit neatly into this schematic and that display disturbed or asymmetric structures are classified as irregular (Irr). Moreover, while the Hubble sequence provides a good description of galaxies with stellar masses $M_\star > 10^{9.5} M_\odot$, lower-mass dwarf galaxies show much greater diversity and less regularity in their morphologies (e.g. Lazar et al., 2024). Many lack the prominent bulges and spiral arm features characteristic of massive galaxies (Governato et al., 2010; Zasov et al., 2021).

As galaxy surveys have grown in size, visual classification of morphology has become increasingly time-consuming. For instance, the Sloan Digital Sky Survey (SDSS) has observed millions of galaxies photometrically (Yasuda et al., 2001). To address this challenge, various approaches have been developed, including citizen science projects such as Galaxy Zoo (Lintott et al., 2011). More recently, machine learning techniques have been applied to automate galaxy morphology classification (e.g. Huertas-Company et al., 2019; Martin et al., 2020). In addition, visual classification can be subjective and is often limited by the spatial resolution and depth of imaging data. Therefore, more objective and quantitative methods based on the analysis of galaxy light profiles have been introduced (e.g. Vika et al., 2015).

Surface Brightness Morphology

A widely adopted approach to classifying galaxy morphology is through fitting a single-Sérsic profile (Sérsic, 1963) to the surface brightness distribution:

$$I(r) = I_e \exp\left\{-b_n\left[\left(\frac{r}{r_e}\right)^{1/n} - 1\right]\right\} \tag{1.1.1}$$

Here, $I(r)$ and I_e are surface brightness at radius r, and the effective radius r_e, respectively, and b_n is a coefficient that depends on the Sérsic index n. A higher Sérsic index indicates a more centrally concentrated light profile, while a lower index corresponds to a profile closer to exponential. Thus, early-type galaxies typically have Sérsic indices ≥ 4, whereas late-type galaxies have lower values. It is also common to fit the light profiles of the bulge and disk components separately to estimate the bulge-to-total (B/T) light ratio. As with whole-galaxy fitting, bulges generally have higher Sérsic indices (e.g., n $\geq$ 4), while disks have lower indices. Galaxies with $B/T = 1$ are purely elliptical, and those with $B/T = 0$ are purely disks.

1.1.3 Star Formation Rate

In addition to morphology, another key property for studying galaxy star forming activity is the star formation rate (SFR), which quantifies the amount of stellar mass a galaxy forms per unit time, expressed in solar masses per year [$M_\odot$ yr^{-1}].

There are many possible observables to trace SFR. Ultraviolet (UV) is commonly used to trace recent star formation ($\leq$ 100 Myr) as short-lived, hot, young stars emit predominantly in the UV (Boissier, 2013). Meanwhile, as the stellar populations evolve, metals are expelled into the interstellar medium (ISM) through stellar feedback such as supernovae, and eventually condense into dust (Inoue, 2011; Santini et al., 2014). This dust absorbs UV photons from young stars and re-emits the energy primarily as infrared (IR) radiation (Kennicutt & Evans, 2012). A more comprehensive method of estimating SFR is to combine UV, IR, and optical data using spectral energy distribution (SED) fitting. This approach assumes that the galaxy's spectrum is a combination of the emission from various galactic components, including stars,

dust in the ISM, and active galactic nuclei (AGN). From this, key physical properties such as SFR, stellar mass, dust content, and star formation history can be inferred (Salim et al., 2016).

Also, as the massive young stars are born within gas clouds, their strong ultraviolet radiation can ionize the surrounding gas. Recombination lines are produced when ions and electrons recombine, making them reliable tracers of the recent star formation (Stahler & Palla, 2004). At low redshift, Hα is the most commonly used recombination line, tracing very recent star formation on timescales of $\sim$ 10 Myr (Kennicutt, 1992). Correcting for dust extinction is also critical when using these lines, often achieved through Balmer decrements (i.e. the ratio Hα/Hβ), which estimates the dust obscuration (Kennicutt & Evans, 2012).

Star Forming Main Sequence

Star formation is fundamentally driven by the gravitational collapse of cold gas clouds. Therefore, massive galaxies that contain more gas are expected to have higher SFRs. This tight and linear correlation between SFR and stellar mass is known as the Star-Forming Main Sequence (hereafter MS; Figure 1.2), and has been observed across a wide range of redshifts (z = 0 $\sim$ 7; Brinchmann et al. 2004; Pannella et al. 2015; Koprowski et al. 2024; Rinaldi et al. 2025). The SFR of star-forming galaxies at low redshift is observed to be lower than those at higher redshifts (Daddi et al., 2007; Sobral et al., 2014), causing the MS to shift upward in the SFR–$M_\star$ plane at higher redshifts. Not all galaxies lie along the MS. Quenched galaxies are commonly defined as those that lie more than 1 dex below the MS (e.g. Genel et al., 2018). As SFR scales with stellar mass, it is also common to normalize the SFR by stellar mass to calculate

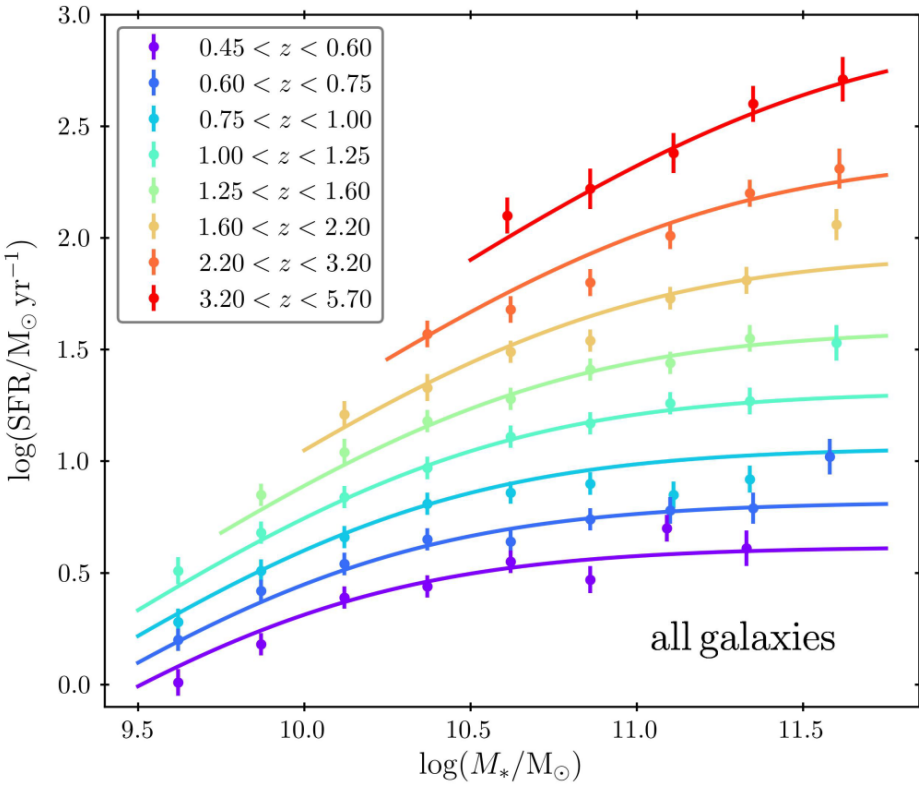

Figure 1.2: The star-forming main sequence of galaxies at $0.45 < z < 5.70$ in observations, colour-coded by redshift. The slope of the main sequence remains relatively constant across redshifts, while the intercept increases with redshift. Image credit: Koprowski et al. (2024)

the specific star formation rate (sSFR). For low-redshift studies ($z < 0.06$), a threshold of $\log(\text{sSFR}) = -11$ [yr^{-1}] is frequently used to classify quenched galaxies, as it approximately corresponds to the local minimum of the bimodal sSFR distribution (see Figure 2 of Kauffmann et al. 2004 and Figure 6 of Wetzel et al., 2012).

Colours

Galaxy colours, defined as the magnitude difference between two photometric bands, can also be used to distinguish star-forming and quenched populations. Figure 1.3

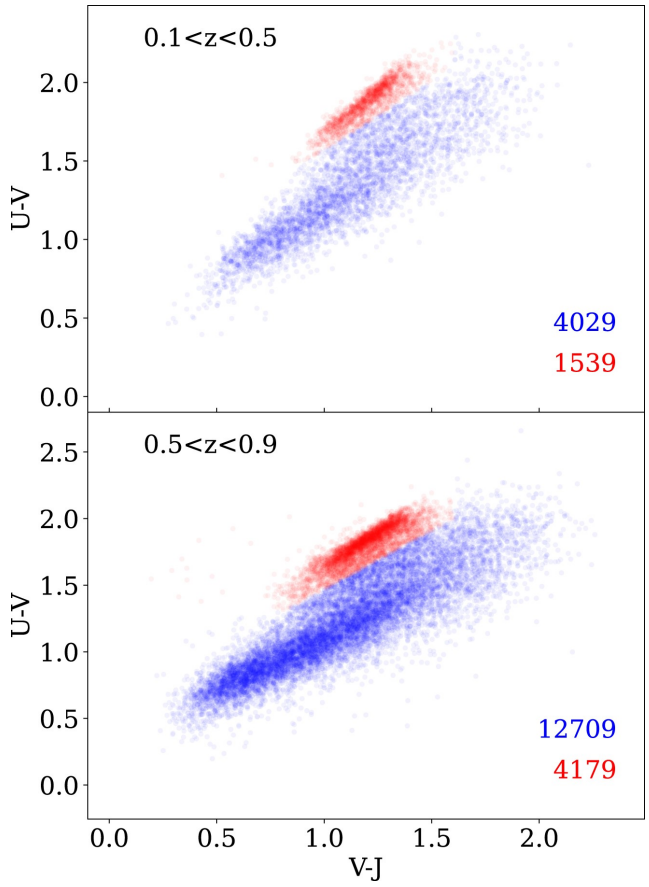

Figure 1.3: Rest-frame UVJ colour diagram from observations of galaxies with stellar mass $\log(M_\star/M_\odot) > 9.5$. Star-forming and quenched galaxies are coloured in blue and red, respectively. Image credit: George et al. (2024)

shows a rest-frame ultraviolet (U), visual (V), and infrared (J) diagram from George et al. (2024), which is commonly used for galaxies at $z \leq 3$ (e.g. Gebek et al., 2025). The U band primarily traces young stellar populations and is highly sensitive to dust attenuation, while the V and J bands are dominated by older, evolved stars (e.g. Gebek et al., 2025). Thus, evolved galaxies with low star formation, low dust content, and older stellar populations appear red in (U-V) and blue in (V-J), occupying the top-left of the diagram. On the other hand, dusty, star-forming galaxies appear red in both (U-V) and (V-J), and are located at the top-right region (Wuyts et al., 2007).

It is well known that galaxy colours, morphology, and star formation are tightly interconnected. Early-type galaxies tend to be redder in colour and are largely quiescent, while late-type galaxies are generally blue and actively forming stars (Schawinski et al., 2014; Fang et al., 2018).

1.2 Galaxy Environments

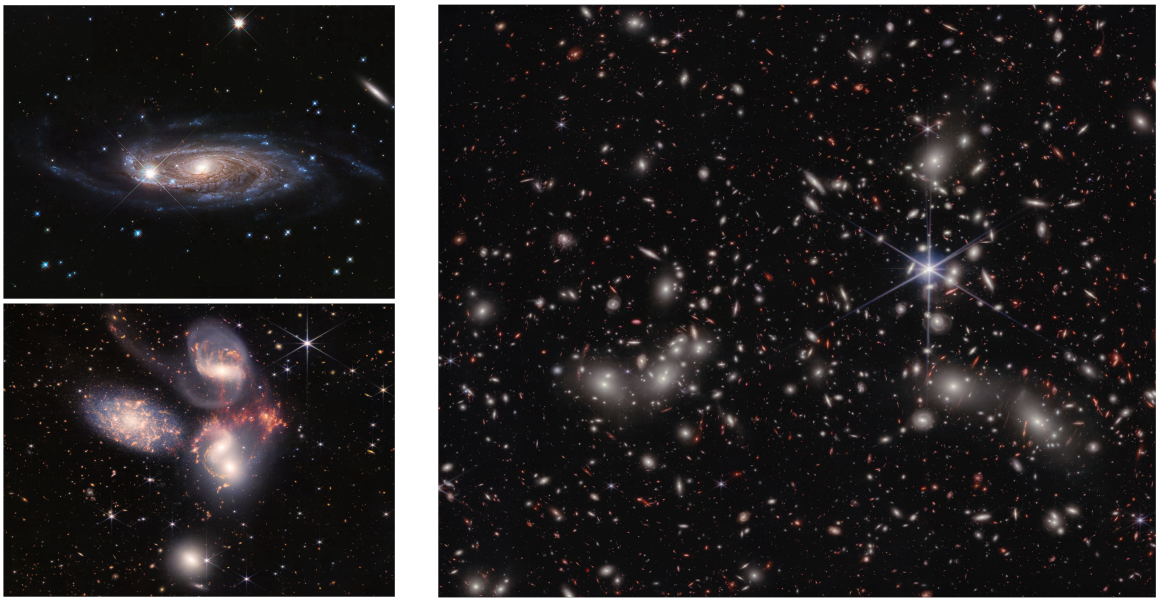

Figure 1.4: Top left: Rubin's Galaxy (Image credit: NASA/ESA/B. Holwerda (University of Louisville)). Bottom left: Stephan's Quintet, a group of 4 galaxies (Image credit: NASA, ESA, CSA, STScI). Right: Pandora Cluster (Image credit: NASA, ESA, CSA, I. Labbe (Swinburne University of Technology), R. Bezanson (University of Pittsburgh), A. Pagan (STScI)).

Galaxies live in a wide range of environments, from relatively isolated systems to galaxy groups, which typically host several to dozens of members and are the most common environments for galaxies, to dense galaxy clusters that host hundreds to thousands of galaxies (e.g. Mamon, 2007; Pillepich et al., 2018a; Pearson et al.,

2021). According to the Λ-Cold Dark Matter model, the large-scale evolution of the universe is shaped by both dark energy (Λ), which drives cosmic acceleration, and cold dark matter, which governs the formation of structure (e.g. Planck Collaboration et al., 2020). In this framework, structure formation proceeds hierarchically: smaller systems merge over time to form progressively larger ones (e.g. Rakhi et al., 2023). This process spans from dwarf galaxies to massive galaxies, and eventually to groups, clusters, and beyond. Despite differences in scale and mass, these gravitationally bound systems share a common structure: a dark matter halo containing a central galaxy located at the local minimum in the potential, surrounded by hot gas and satellite galaxies. The stellar mass of the central galaxies can be interpreted using the stellar-to-halo mass relation (see Figure 1.5). For example, halos with total mass $\log(M_{halo}/M_{\odot}) \sim 12$ are expected to host Milky Way–like central galaxies. Satellite galaxies are subject to additional environmental influences that affect their evolution, leading to distinct evolutionary paths compared to central galaxies (see Section 1.3).

Field Central Galaxies

Central galaxies of halos that host no comparably sized companions/satellites (e.g. < 0.1 times the central) can be defined as field/isolated galaxies (Yang et al., 2007; Lacerna et al., 2014; Winkel et al., 2021; Celiz et al., 2025). Their evolution is less perturbed by external mechanisms such as interaction with neighbor galaxies and environment. Thus, they provide excellent laboratories to study how internal mechanisms, such as feedback from AGN and stellar evolution, drive galaxy evolution.

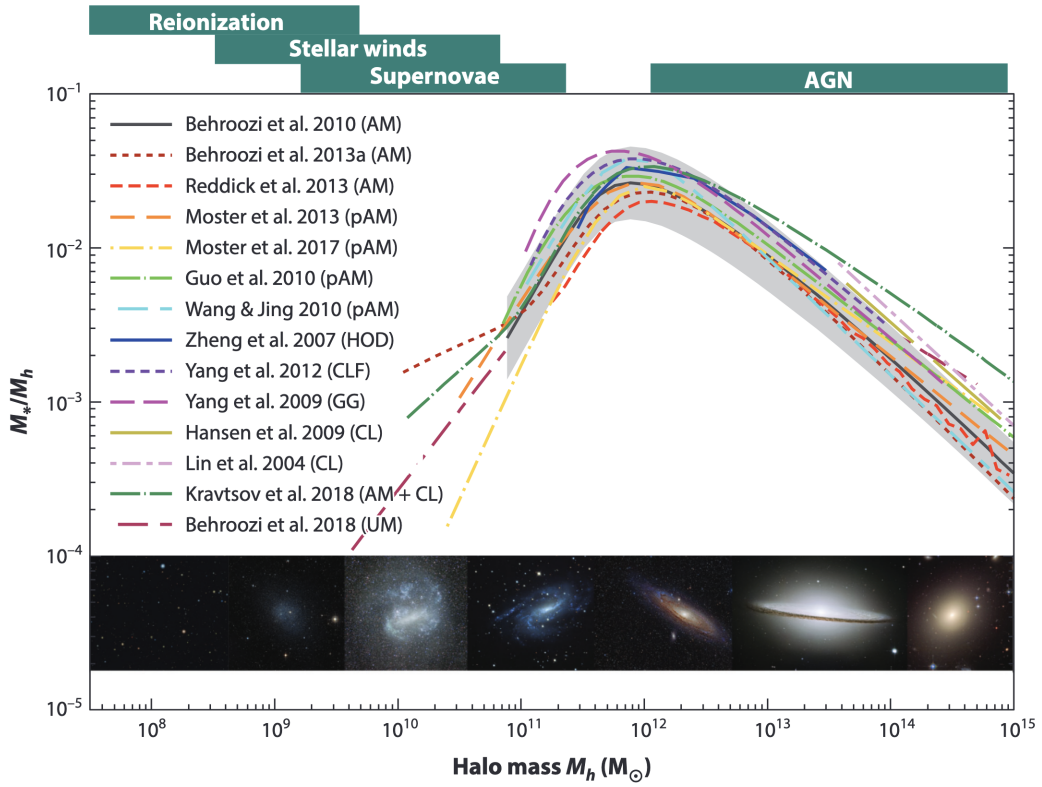

Figure 1.5: The Stellar-to-halo mass ratio of central galaxies. The key physical processes that may drive gas ejection, heat the gas, or suppress star formation at the corresponding mass scales are highlighted at the top of the figure. In low-mass dwarf galaxies, shallow gravitational potentials allow stellar outflows to efficiently expel gas. In contrast, high-mass galaxies are primarily regulated by AGN feedback. Image credit: Wechsler & Tinker (2018).

Groups and clusters

Over 60% of the galaxies in the local universe are found within groups and clusters (Tully, 1987). While there is no universal definition of the two, halos with total masses $\log(M_{halo}/M_\odot) \geq 14$ and $13 \leq \log(M_{halo}/M_\odot) < 14$ are generally considered clusters and groups, respectively.

Clusters are massive bound structures in the universe, hosting 50 (poor) to over a thousand (rich) satellite galaxies. Galaxy clusters are characterized by high galaxy velocity dispersions, typically around 800 km/s and exceeding 1000 km/s in rich systems (Carroll & Ostlie, 2017). A prominent component of clusters is the hot intracluster medium (ICM), composed of ionized gas with temperatures ranging from 10^7 to 10^8 K, which emits strong X-ray radiation. The ICM density is observed to increase towards the central region of the clusters. As a result, satellites closer to the center are expected to be more susceptible to the interaction with the ICM (more details on Section 1.3.2).

Groups typically contain fewer than $\sim$ 50 members, with velocity dispersions between $150 \leq \sigma/\text{km s}^{-1} \leq 450$ and virial radii of $0.3 \leq R_{200}/\text{Mpc} \leq 1$ (Mamon, 2007). With the advent of more sensitive X-ray telescopes, groups have also been observed to host a diffuse intra-group medium. However, the intra-group medium is generally cooler and less dense than the ICM (Cortese et al., 2021).

1.3 Mechanisms Behind Galaxy Evolution

At a fixed stellar mass, satellites within groups and clusters have long been observed to exhibit different properties compared to field galaxies, highlighting the significant

role of environment in galaxy evolution. The morphology–density relation, first observed by Hubble & Humason (1931) and later quantified by Dressler (1980) and others (Goto et al., 2003; van der Wel et al., 2010), was among the earliest pieces of evidence showing environmental influence on galaxy evolution. It demonstrates that the fraction of early-type galaxies increases as local galaxy density increases.

Galaxies in high-density environments have also been found to have lower star formation rates compared to those in low-density regions (Kauffmann et al., 2004). The fraction of star-forming galaxies in the field population is higher than that of galaxies with similar mass residing in groups and clusters (Figure 1.6; Wetzel et al. 2012). Sulentic et al. (2006) find that among the 1050 galaxies in the Catalog of Isolated Galaxies (CIG), 82% are late-type and only around 14% are early-type. This dependence of galaxy morphology and star formation on environment has now been observed in high-redshift clusters ($z > 1.3$) as well (e.g. Mei et al., 2023).

Star formation is initiated by the gravitational instability of cold, dense gas clouds. Accordingly, any mechanism capable of ejecting gas, heating it, removing it from the system, or introducing additional pressure support against gravitational collapse can act to suppress star formation. Meanwhile, the same mechanisms could be responsible for changing galaxy morphology as well. In the following section, we outline the principal processes influencing both star formation and galaxy morphology, categorizing them broadly into internal and environmental mechanisms.

1.3.1 Internal Processes

Internal processes regulate star formation and gas content in both central and satellite galaxies. As shown in Figure 1.5, the dominant mechanisms vary with galaxy mass. In

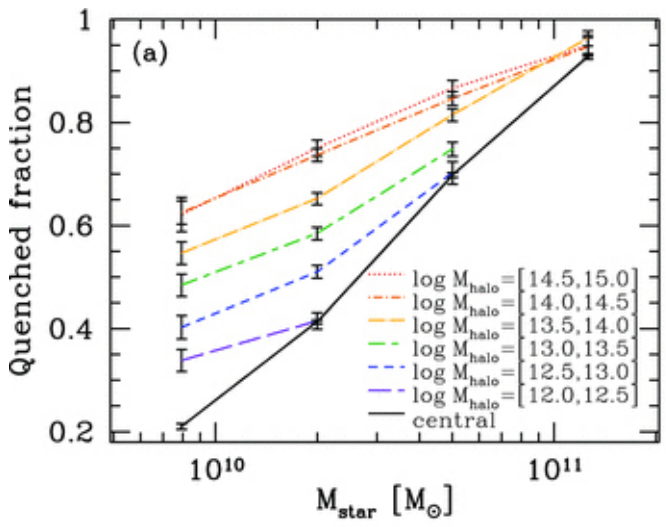

Figure 1.6: Fraction of local galaxies in SDSS with log(sSFR) < -11 [yr^{-1}] as a function of stellar mass for field galaxies (solid) and satellites (dashed and dot-dashed) across different halo masses. Image credit: Wetzel et al. (2012)

low-mass galaxies, stellar feedback can efficiently expel gas due to their shallow gravitational potentials. In contrast, in high-mass systems, active galactic nuclei (AGN) feedback becomes the dominant mechanism, suppressing star formation through gas heating and removal (Zinger et al., 2020).

Stellar Feedback

Stellar feedback plays a central role in regulating the star formation process by injecting energy, momentum, and mass back into the interstellar medium (ISM) throughout stellar evolution. This feedback is primarily driven by ionizing radiation and stellar winds from young, massive stars, and later by supernova (SN) explosions once these stars reach the end of their lifecycles (White & Frenk, 1991; Governato et al., 2007). The UV radiation can heat up, ionize, and expand the surrounding gas (e.g. Rautio et al., 2022), thus limiting the efficiency of star formation. SN feedback releases an

enormous amount of energy and momentum, which leads to expansion of surrounding ISM, creating superbubbles. Meanwhile, SN can lead to powerful outflows that expel gas from the galactic disk if the gravitational potentials are shallow (Vogelsberger et al., 2013).

AGN Feedback

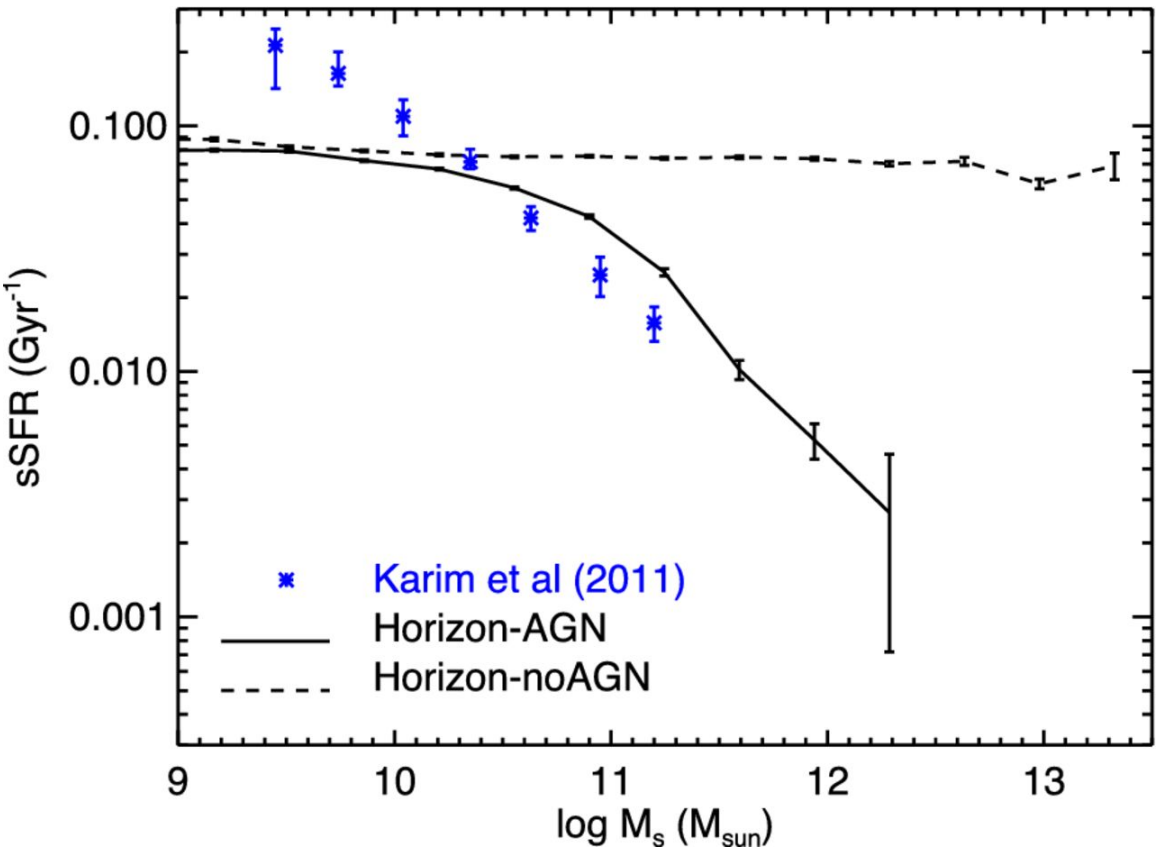

Figure 1.7: The specific star formation rate as a function of stellar mass for galaxies in observations (blue), a simulation with AGN feedback (solid line), and a simulation without AGN feedback (dashed line). Image credit: Dubois et al. (2016)

AGN feedback is powered by gas accretion onto the central SMBH of galaxies (e.g. Torrey et al., 2014). It can eject gas from the galaxy and simultaneously inhibit

the accretion of CGM, thereby halting star formation (e.g. van de Voort et al., 2017; Zinger et al., 2020, see also Figure 1.8). Simulation-based studies have shown that AGN feedback is necessary for regulating galaxy star formation in order to reproduce observed galaxy property distributions, such as the sSFR distribution (see Figure 1.7), particularly at the high-mass end (Dubois et al., 2013, 2016). Since AGN feedback is triggered by gas inflow to the central SMBH, any mechanism that drives outflow or halts gas inflow can enhance or suppress the feedback, such as galaxy-galaxy interactions and ram pressure (see Sections 1.3.2).

Morphological Quenching

Unlike the two mechanisms mentioned above, which remove gas or halt gas inflow, some studies argue that bulge growth can suppress star formation by stabilizing gas clouds against fragmentation (Martig et al., 2009; Su et al., 2025). As shown by Gensior et al. (2020), spheroidal components contribute to turbulence and increase gas velocity dispersion, which enhances pressure support in the galactic centre and thereby stabilizes the interstellar medium (ISM).

1.3.2 Environmental

Galaxies residing in high-density regions like massive groups and clusters experience external influences from both other galaxies and the hot halo gas between the galaxies.

Mergers and Flyby Interaction

Galaxy mergers are commonly classified based on the stellar mass ratio of the interacting systems: major mergers involve galaxies of comparable mass (mass ratio less

than 1:4), while minor mergers refer to interactions where one galaxy is significantly less massive (mass ratio greater than 1:4) (e.g. McAlpine et al., 2020; Kaviraj, 2025). Major mergers can enhance star formation, especially when both galaxies are gas-rich. In such cases, they can trigger intense starbursts by driving gas inflows toward the galactic center. The rapid consumption of gas often leads to subsequent quenching (Lin et al., 2023). These inflows can also fuel the AGN, thereby enhancing AGN feedback (e.g. Weinberger et al., 2018). Additionally, major mergers can transform disk galaxies into spheroidal systems, as violent relaxation during the interaction redistributes stellar orbits (e.g. Dubois et al., 2016; Lagos et al., 2017; Gillman et al., 2019). Similarly, minor mergers can also stimulate star formation. The tidal forces can funnel gas and material from the smaller companion towards the central region of the primary galaxy. Minor mergers can also alter the morphology of the primary galaxy, creating features like tidal arms and contributing to bulge-growth (Bédorf & Portegies Zwart, 2013). Despite being less violent, minor mergers are more common during galaxy evolution than major mergers and play an important role in bulge assembly (Rizzo et al., 2018). In addition, high-relative velocity or fly-by interactions that do not result in a merger can still significantly affect galaxy evolution. Simulations have shown that, especially during a satellite's pericentric passage, loosely bound gas and stars can be tidally stripped, transforming galaxies into passive, dispersion-dominated systems (van den Bosch et al., 2016; Joshi et al., 2020).

Starvation and Strangulation

Starvation refers to the cessation of cold gas replenishment in a galaxy's disk, a key mechanism that can lead to the eventual quenching of star formation. Under

normal conditions, galaxies sustain star formation by accreting cold gas from their surrounding halo, including the CGM and intergalactic medium (IGM) (e.g., Wetzel et al., 2012). However, when a galaxy becomes a satellite within a more massive halo, it is no longer located at the center of the gravitational potential well. As a result, the surrounding IGM no longer accretes onto the satellite but instead flows toward the center of the host halo (Rodríguez-Cardoso et al., 2025). While orbiting within the host halo, satellites are subjected to external pressure from the intracluster or intragroup medium (ICM/IGM), known as ram pressure, which depends on both the galaxy's velocity relative to the medium and the medium's density (Gunn & Gott, 1972). This pressure can strip the satellite's hot gas halo, a process known as strangulation, thereby cutting off the supply of cooling gas that would otherwise replenish the cold gas reservoir (e.g., Maier et al., 2016; Cortese et al., 2021). As satellites approach to the pericenter of the host halo, tidal interactions with the central galaxy, as discussed in Section 1.3.2, can further contribute to the removal of the hot gas halo. Without ongoing replenishment, the remaining cold gas is eventually consumed, leading to the cessation of star formation. Assuming galaxies maintain a constant star formation rate after infall, the quenching timescale associated with starvation/strangulation is determined by the gas depletion time, which typically ranges from 1 to 10 Gyrs (Cortese et al., 2021; Rodríguez-Cardoso et al., 2025).

Ram Pressure Stripping

Instead of only removing the hot gas halo, ram pressure can become strong enough to strip the cold ISM from the galaxy disk if the density of the surrounding medium and/or the relative velocity between the galaxy and the medium is high. The process

Figure 1.8: Left: NGC 512, a galaxy with lobes and jets ejected from the central SMBH. Image credit: ESO/WFI (Optical); MPIfR/ESO/APEX/A.Weiss et al. (Submillimetre); NASA/CXC/CfA/R.Kraft et al. (X-ray). Right: a jellyfish galaxy (ESO 137-001) with ram pressure stripped tail. Image credit: X-ray: NASA/CXC/UAH/M.Sun et al; Optical: NASA, ESA, & the Hubble Heritage Team (STScI/AURA)

is known as ram pressure stripping (RPS). Although ram pressure is not strong enough to directly alter the stellar component, it can strip gas from the outer regions of a galaxy, leading to outside-in quenching of star formation (Kolcu et al., 2022). As the outer disk fades due to the cessation of star formation, the galaxy appears more bulge-dominated and, consequently, more like an early-type system (e.g., Bundy et al., 2010).

RPS is expected to be more pronounced during a galaxy's first infall into a cluster (Ricarte et al., 2020; Rohr et al., 2023). Galaxies strongly affected by RPS often exhibit extended tails of neutral hydrogen or Hα emission opposite to their direction of motion, known as jellyfish galaxies (see Figure 1.8). Since RPS involves removal

of the star-forming gas, it can lead to rapid quenching of star formation, typically on timescales shorter than 1 Gyr (Boselli et al., 2014). Some studies suggest that ram pressure may trigger gas inflows toward the central SMBH, fueling AGN activity (Ricarte et al., 2020; Kurinchi-Vendhan et al., 2025).

1.4 Cosmological Simulations

Recent years have seen incredible technological progress in observational astronomy, including the launching of the James Webb Space Telescope and the completion of Atacama Large Millimeter Array. We can now study huge samples of galaxies across cosmic time with a wide range of wavelengths. These observations are leading to powerful discoveries, but there are fundamental limitations to observations. Most importantly, observations can only capture a moment in time, making it impossible to trace the evolution over time of individual galaxies. In addition, we see objects in projection on the sky and it is hard to understand their true 3D structure and motions. To overcome these challenges, numerical simulations serve as a powerful tool, which offers full access to spatial, velocity, and temporal information. Large cosmological hydrodynamic simulations, such as Horizon-AGN (Dubois et al., 2014), EAGLE (Schaye et al., 2015), and IllustrisTNG (Springel et al. (2018); Pillepich et al. (2018b); Nelson et al. (2018); Marinacci et al. (2018); Naiman et al. (2018); hereafter TNG) are widely used in galaxy and cosmic evolution studies. They replicate the general characteristics of the entire galaxy population by incorporating complex physical processes without limiting the focus to a single galaxy system or specific phenomena. For instance, TNG300-1, the largest volume simulation ($\sim$300Mpc) in the TNG suite, contains numerous high-density environments (see Table 2.1).

Cosmological hydrodynamic simulations solve both the equations of gravity and the equations of fluid dynamics at each time step for dark matter and baryons, typically using millions to billions of particles to represent the matter in the universe. More recently, magnetic fields have also been included in some simulations to capture their influence on galaxy formation. Despite these advances, computational limitations prevent simulations from resolving all physical scales. Subgrid models are used to account for processes that occur below the simulation's resolution, such as star formation, the evolution of stars, feedback from AGN and gas cooling (e.g. Pillepich et al., 2018a).

1.5 Motivation and Outline

Oxland et al. (2024), hereafter O24, show that as galaxies fall into groups and clusters they become more bulge-dominated and quenched. Furthermore, the fraction of bulge-dominated, quenched galaxies increases with the time since a galaxy's infall into the group or cluster environment. O24 also presented evidence that quenching preceded morphological transformation, based on the shorter timescale associated with quenching compared to structural evolution in both environments. Building upon these findings, this thesis further investigates how the SFR and morphology of galaxies evolve over time using the state-of-the-art magnetohydrodynamic cosmological simulation IllustrisTNG. The simulation provides all six phase-space dimensions of galaxy information (three spatial positions and three velocity components), as well as temporal information from successive snapshots and intrinsic galaxy properties such as stellar mass and star formation rate. Together, these allow us to trace

galaxy transformations as halos assemble across cosmic time. Moreover, by identifying discrepancies between observations and simulations, we can better isolate the assumptions driving the differences and refine theoretical models.

In Chapter 2, we describe the simulation data and methodology used in this thesis. This includes an overview of the IllustrisTNG simulation, the supplementary catalogs of galaxy morphology and star formation rates, the definitions and calculations of both observationally equivalent and true infall times, and the procedure for fitting the star-forming main sequence across redshift.

We present the results in Chapter 3. In Sections 3.1 and 3.2, we first examine the consistency between the observationally equivalent and true infall times. We then compare the quenched and early-type fractions as a function of infall time in groups and clusters between TNG and the SDSS results from O24. In Section 3.3, we investigate how stellar mass, offset from the star-forming main sequence, gas mass, and bulge-to-total mass ratio evolve as galaxies first enter their $z = 0$ host halos in TNG.

In Chapter 4, we discuss possible reasons why the quenched fraction in TNG is higher than in SDSS observations, how pre-processing alters galaxy star formation and morphology, and the mechanisms responsible for quenching galaxies with $M_\star > 10^{10} M_\odot$ in TNG. Finally, in Chapter 5, we summarize the main findings of this thesis and highlight their implications for understanding galaxy evolution.

Chapter 2

Data and Methods

In this chapter, we begin by describing the IllustrisTNG simulation, followed by the definition of galaxy environments. We then introduce the supplementary catalogs containing star formation rates and morphological classifications of TNG galaxies, and outline the procedure for fitting the star-forming main sequence. Next, we define the true infall time, provide a detailed description of the sample selection, and finally calculate the observationally accessible infall time using projected phase space.

2.1 The IllustrisTNG Simulation

The TNG project (Naiman et al., 2018; Nelson et al., 2018; Marinacci et al., 2018; Pillepich et al., 2018b; Springel et al., 2018) is a suite of state-of-the-art cosmological hydrodynamical simulations that builds upon the success of the original Illustris simulation, incorporating additional physical models such as magnetic fields and an updated black hole feedback model (Pillepich et al., 2018a; Weinberger et al., 2018).

	TNG50	TNG100	TNG300
Volume [Mpc^3]	51.7^3	110.7^3	302.6^3
$m_{baryon}[\mathrm{M}_\odot]$	8.5×10^4	1.4×10^6	1.1×10^7
$m_{DM}[\mathrm{M}_\odot]$	4.5×10^5	7.5×10^6	5.9×10^7
N_{groups}	23	168	3545
$N_{clusters}$	1	14	280

Table 2.1: Volume, baryon particle mass, dark matter particle mass, and the number of groups ($13 \leq \log(\mathrm{M}_{halo}/\mathrm{M}_\odot) < 14$) and clusters ($\log(\mathrm{M}_{halo}/\mathrm{M}_\odot) \geq 14$) in the three TNG volumes at z = 0

It includes three volumes, TNG50, TNG100, and TNG300, each with different resolutions and sizes (see Table 2.1). All three volumes adopt the same set of cosmological parameters, based on the results from Planck Collaboration XIII (Planck Collaboration et al., 2016): the baryonic density is $\Omega_b = 0.0486$, the total matter density is $\Omega_m = \Omega_b + \Omega_{DM} = 0.3089$, the dark energy density is $\Omega_\Lambda = 0.6911$, and the Hubble constant is $H_0 = 67.74$ km s^{-1} Mpc^{-1}.

Although cosmological simulations can resolve large-scale structure in remarkable detail, they rely on sub-grid models for physics below the resolution scale (e.g. Wechsler & Tinker, 2018). We summarize key sub-grid models employed in TNG (Pillepich et al., 2018a):

- Star formation: When the gas density exceeds $n_H \simeq 0.1$ cm^{-3}, the instantaneous SFR is given by SFR $\propto \frac{M_{cold}}{t(\rho)}$, where M_{cold} is the cold gas mass estimated by the subgrid model, and $t(\rho)$ is the density-dependent timescale for star formation. This timescale is tuned to reproduce the Kennicutt-Schmidt relation (Kennicutt, 1998), which relates the SFR surface density (Σ_{SFR} [$\mathrm{M}_\odot$ yr^{-1} kpc^{-2}]) to the gas surface density (Σ_{gas} [$\mathrm{M}_\odot$ kpc^{-2}]) as $\Sigma_{\mathrm{SFR}} \propto \Sigma_{\mathrm{gas}}^{1.4}$. Gas is then stochastically converted into stellar particles that follow a Chabrier initial mass function

(Chabrier, 2003), as implemented in the star formation model of Springel & Hernquist (2003) (see also Donnari et al. 2019).

- Stellar evolution and feedback: Each stellar particle corresponds to a single-age stellar population. As stellar populations evolve, they return mass and metals to the surrounding ISM through three feedback channels: asymptotic giant branch (AGB) stars, Type Ia supernovae (SNe), and Type II SNe. In brief, stars with masses in the range of $\sim 1 - 8$ $M_\odot$ are assumed to eventually enter the AGB phase, while those > 8 $M_\odot$ undergo core-collapse supernovae (Type II SNe). The rate of Type Ia SNe, however, depends only on a delay time distribution that follows a power law in time with a minimum delay of about 40 Myr, the approximate main sequence lifetime of an 8 $M_\odot$ star. The amount of mass returned at each time step depends on the metallicity and age of the stellar population (Vogelsberger et al., 2013; Naiman et al., 2018). In addition, the energy/momentum associated with Type II SNe is modeled separately via a kinetic galactic wind launched from star-forming gas, where the total available wind-driving energy injection rate scales with the instantaneous SFR and is modulated by the metallicity of the star-forming gas cell (see Section 2.3.2 of Pillepich et al. (2018a) for more details).

- Gas cooling and heating: Gas cooling depends on metallicity, density, temperature, and redshift. It is further modulated by radiation from a uniform ionizing ultraviolet background whose intensity changes with redshift, with self-shielding taken into account in dense regions of the interstellar medium (Pillepich et al., 2018a), as well as by radiation from nearby active galactic nuclei (AGN).

- Feedback from supermassive black holes (SMBHs): In TNG, SMBHs operate in two feedback modes depending on their Eddington ratio (the ratio of the accretion rate to the Eddington accretion rate) and a switching threshold that depends on black hole mass, χ ($\chi = 0.1$ if $M_{BH} > 10^{8.85} M_{\odot}$; see Equation 4 in Weinberger et al. 2018). At low accretion rates (Eddington ratio $< \chi$), the kinetic feedback injects momentum to the surrounding gas. At higher accretion rates, thermal feedback heats up the surrounding gas (e.g., Barai et al. 2014).

In TNG, structures are generally classified into two categories: halos and subhalos. Halos are identified using a friends-of-friends (FoF) algorithm applied to the dark matter particles, with a linking length set to 0.2 times the mean dark matter particle separation (Dolag et al., 2009). Within each FoF halo, gravitationally bound overdense regions are identified by the SUBFIND algorithm and are classified as subhalos (Springel et al., 2001). In principle, any subhalo with non-zero stellar mass can be considered a galaxy, although analyses often adopt a minimum stellar particle threshold to ensure adequate resolution (e.g., Pillepich et al., 2018a). The most massive galaxy within each FoF halo is identified as the central galaxy (hereafter central), while all other galaxies within the same halo are considered satellite galaxies (hereafter satellites). Figure 2.1 illustrates how SUBFIND identifies subhalos.

Numerous studies have shown that TNG successfully reproduces a wide range of galaxy properties in agreement with observations. For instance, Nelson et al. (2018) show that low-redshift galaxies in TNG have a colour bimodality consistent with SDSS observations (Figure 2.2). Rodriguez-Gomez et al. (2019) measure Sérsic indices from mock images (Section 2.3.3) of TNG100 galaxies and find good agreement with Pan-STARRS observations for galaxies with $\log(M_{\star}/M_{\odot}) > 9.8$, representing a significant

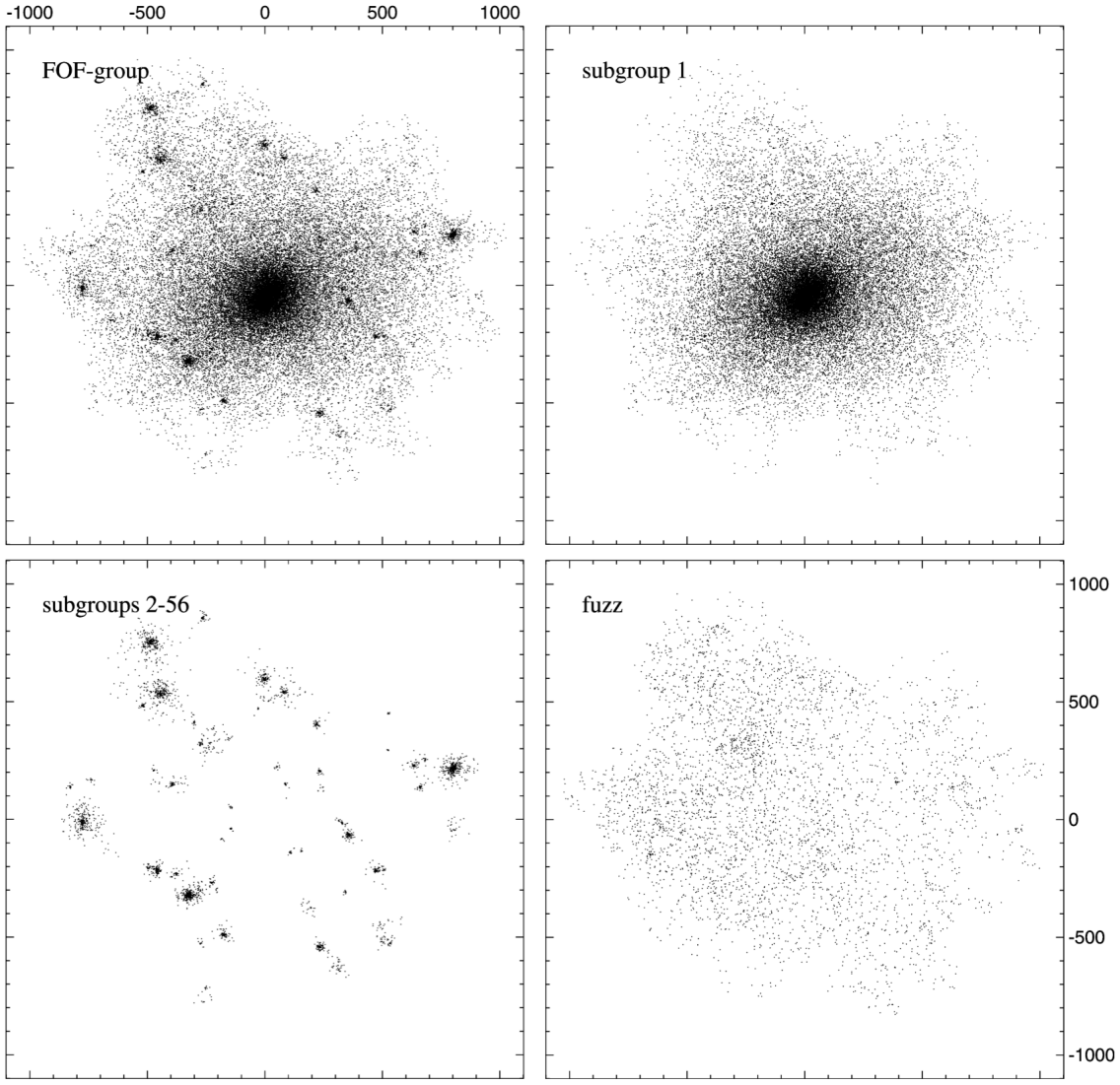

Figure 2.1: Illustration of how SUBFIND identifies subhalos. The top-left panel shows all particles within the entire FoF group. Within this group, SUBFIND detects 56 subhalos. The central (most massive) galaxy and the 55 satellites are shown in the top-right, and bottom-left panels, respectively. "Fuzz" refers to particles that are not bound to any subhalos. Image credit: Springel et al. (2001)

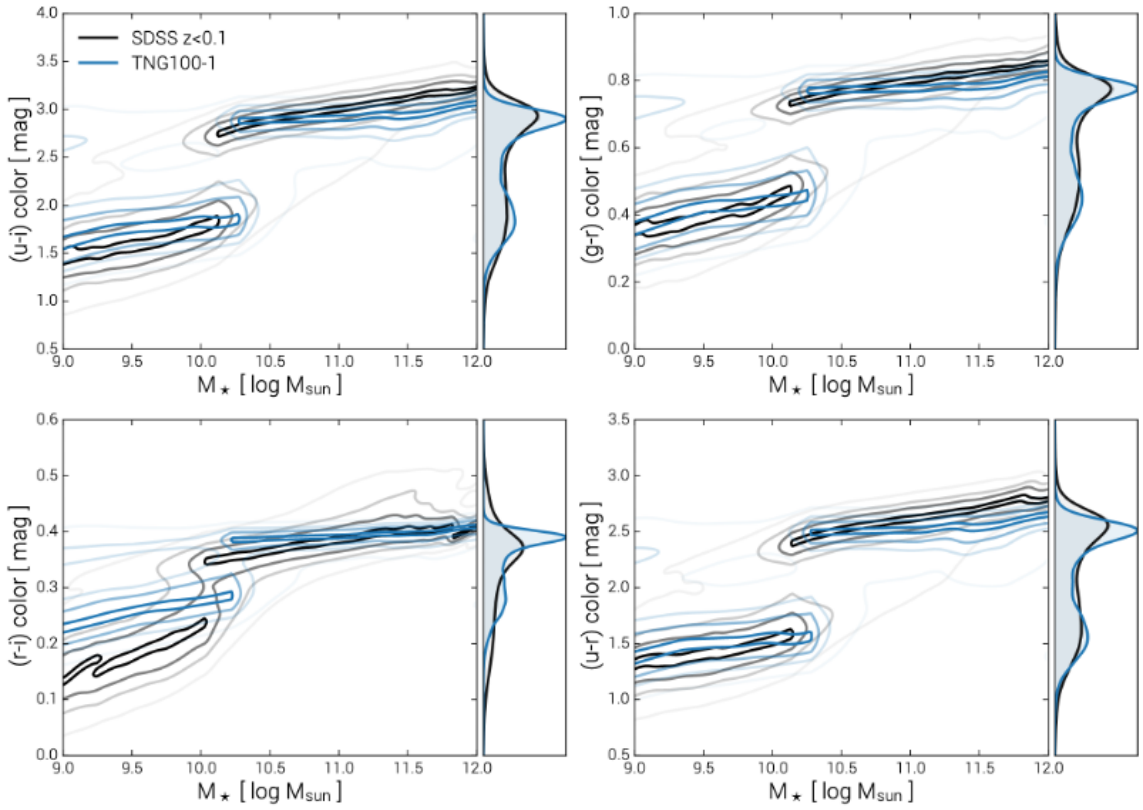

Figure 2.2: Colour-mass plane of central galaxies in TNG100 (blue) and SDSS (black). The panels show different colours: top left (u-i), top right (g-r), bottom left (r-i), and bottom right (u-r). The TNG100 colour distributions generally agree with SDSS observations and successfully reproduces the colour bimodality seen in SDSS.

Image credit: Nelson et al. (2018), their Fig 3.

improvement over the original Illustris simulation (Figure 2.3). Additionally, Donnari et al. (2021b) show that the quenched fractions of both central and satellite galaxies in TNG at low redshift ($z < 0.7$) align well with various observational results across a wide stellar mass range ($9 \leq \log(M_\star/M_\odot) < 12$; Figure 2.4).

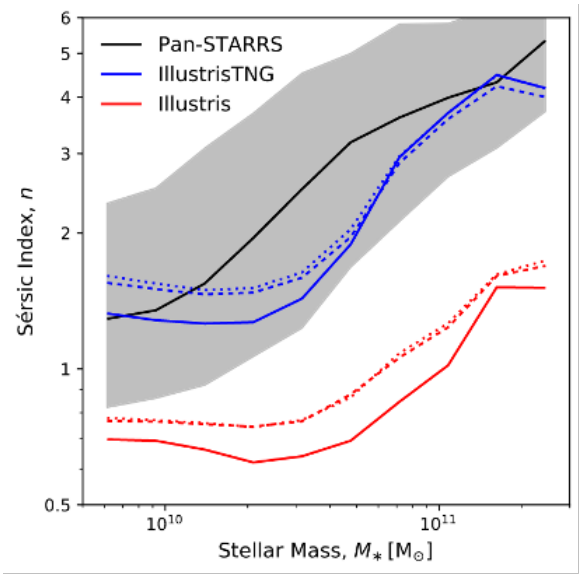

Figure 2.3: Median Sérsic index as a function of galaxy stellar mass in TNG100-1 (blue), Illustris (red), and Pan-STARRS observations (black). The grey shaded region represents the 16th to 84th percentile range of the Pan-STARRS sample. Compared to Illustris, TNG100 demonstrated improved agreement with observed galaxy morphologies. Image credit: Rodriguez-Gomez et al. (2019)

2.2 Galaxy Environments

Galaxy groups and clusters are defined as halos with total mass in the ranges $13 \leq \log(M_{halo}/M_\odot) < 14$ and $\log(M_{halo}/M_\odot) \geq 14$ at $z = 0$, respectively. Here, the halo mass refers to the total mass enclosed within a sphere whose mean density is 200 times the critical density of the Universe. When comparing with the O24 results, the central galaxy of a halo is classified as isolated if the halo contains only one galaxy, or if the most massive satellite has a stellar mass $\leq 1\%$, and the total stellar mass of all satellites is $\leq 5\%$, of the central galaxy's stellar mass.

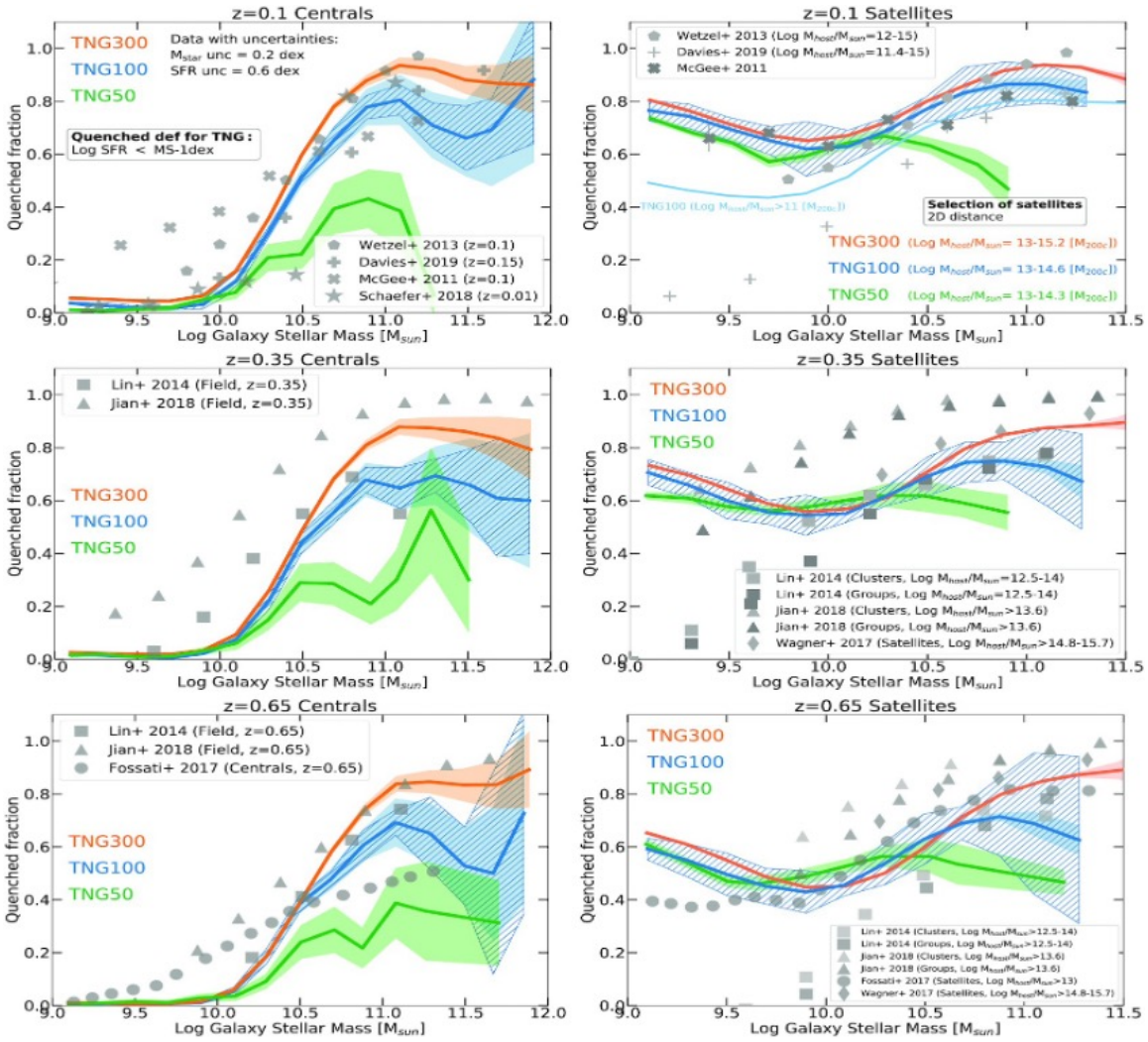

Figure 2.4: The quenched fraction (QF) as a function of stellar mass in TNG at low redshift (top: z = 0.1. Middle: z = 0.35. Bottom: z = 0.65). Left: central galaxies only. Right: satellite galaxies only. The orange, blue, and green curves represent the QF in TNG300, TNG100, and TNG50, respectively. Observational results are overlaid using various grey symbols. Image credit: Donnari et al. (2021b)

2.3 Galaxy Properties

Throughout this work, unless otherwise specified, all galaxy properties are measured within twice the stellar half-mass radius, which encloses half of the total stellar mass of the galaxy, ensuring the focus remains on the primary stellar component.

2.3.1 Star formation rate

The SFR mentioned in Section 2.1 traces the "instantaneous" star formation activity of simulated galaxies, which is not directly observable. SFRs derived from observations are averaged over specific timescales, depending on the observational bands used (see Section 1.1.3). Thus, to better compare with observations, we use the time-averaged SFR catalog for TNG galaxies (Pillepich et al., 2019; Donnari et al., 2019), which tracks the stellar mass formed over the past 10, 50, 100, 200, and 1000 Myr. Each time-averaged SFR is denoted as $\mathrm{SFR}_{\mathrm{timescale}}$ (e.g., SFR_{1000}, SFR_{100}). In TNG100, the minimum resolvable SFRs corresponding to each timescale are: $\log(\mathrm{SFR}\ [\mathrm{M}_\odot\ \mathrm{yr}^{-1}]) = -1.15, -1.85, -2.15, -2.46$, and -3.15, respectively. Galaxies with SFRs below these thresholds are assigned an SFR of zero in the simulation (Donnari et al., 2019; McDonough et al., 2023). Throughout this work, we assign $\log(\mathrm{SFR}\ [\mathrm{M}_\odot\ \mathrm{yr}^{-1}]) = -4$ to galaxies with zero SFR at $z = 0$.

2.3.2 Star Forming Main Sequence at Different Redshifts in TNG

The SFMS evolves with redshift. We fit the SFMS independently at 11 redshifts: $z = 0$, 0.26, 0.5, 0.76, 1, 1.25, 1.50, 1.74, 2, 2.58, and 3.49. At each redshift, following

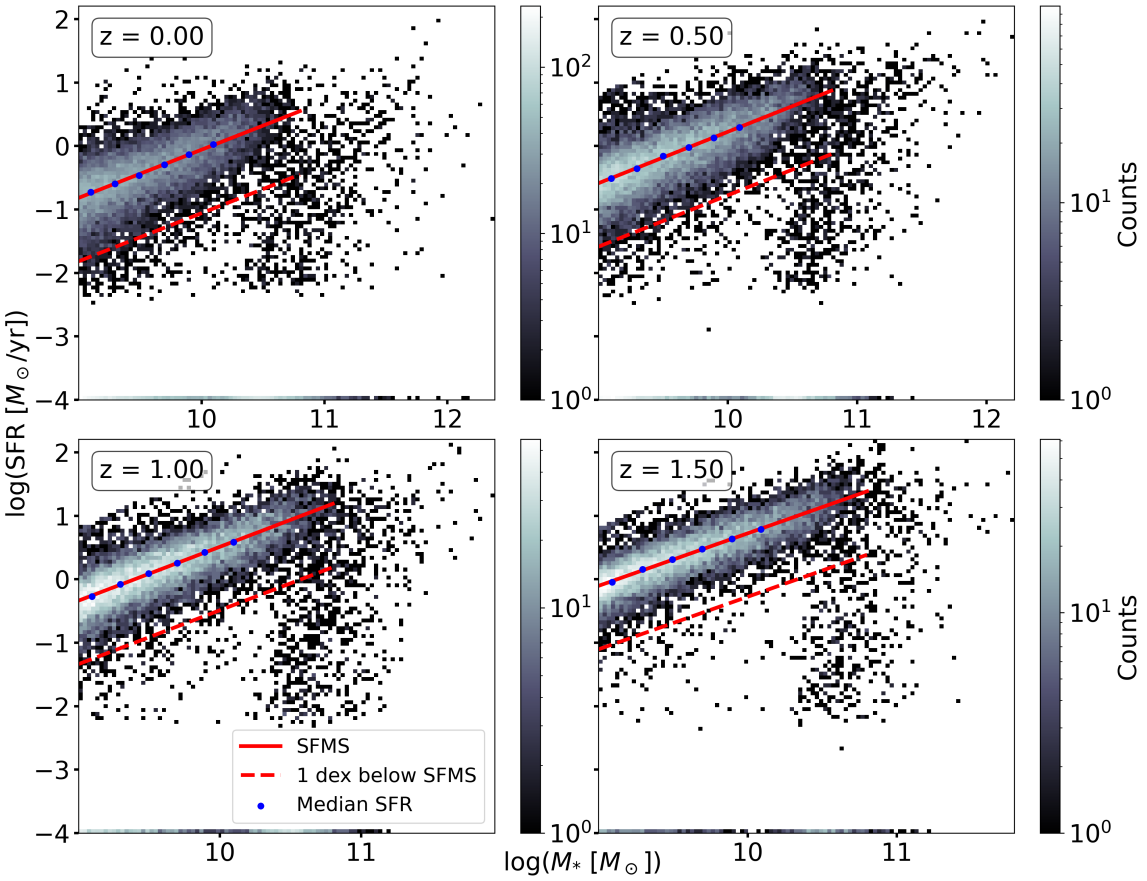

Figure 2.5: SFMS at four redshifts in TNG100 using SFR_{200}. Top left: z = 0. Top right: z = 0.5. Bottom left z = 1. Bottom right: z = 1.5. Galaxies with zero SFR are assigned $\log(SFR_{200}\ [M_\odot\ yr^{-1}])$ = -4 so that their distribution is visible in the plots. Solid red lines indicate the fitted SFMS, while dashed lines represent 1 dex below the SFMS. Blue dots show the median SFR in each stellar mass bin used for the fit. While the slope remains consistent across redshifts, the intercept increases with redshift.

Donnari et al. (2019), we first select galaxies with stellar mass between 10^9 and $10^{10.2}$ $M_\odot$, as the MS is approximately linear within this range, and divide them into six mass bins. In each bin, we compute the median SFR and iteratively remove galaxies with SFR more than 1 dex below the median, until convergence. A linear fit is then performed on the resulting medians, centering the x-axis at $\log(M_\star/M_\odot) = 10.2$. This fit is then extrapolated to higher stellar mass. Figure 2.5 shows the fitted SFMS at four example redshifts, with all 11 shown in Figures A.1 and A.2. We fit the SFMS using the following form:

$$\log\left(\frac{\mathrm{SFR}}{M_\odot\ \mathrm{yr}^{-1}}\right) = \alpha(z)\left(\log\left(\frac{M_\star}{M_\odot}\right) - 10.2\right) + \beta(z) \tag{2.3.1}$$

where both the slope $\alpha(z)$ and intercept $\beta(z)$ are expected to vary with redshift. To examine this dependence, we plot $\alpha(z)$ and $\beta(z)$ as functions of redshift (Figure 2.6). For SFR_{200}, we find that the correlations are best described by the following relations:

$$\alpha(z) = 0.8 \tag{2.3.2}$$

$$\beta(z) = -0.057z^2 + 0.618z + 0.096 \tag{2.3.3}$$

We determine the SFMS at each redshift using the fitted relations for $\alpha(z)$ and $\beta(z)$.

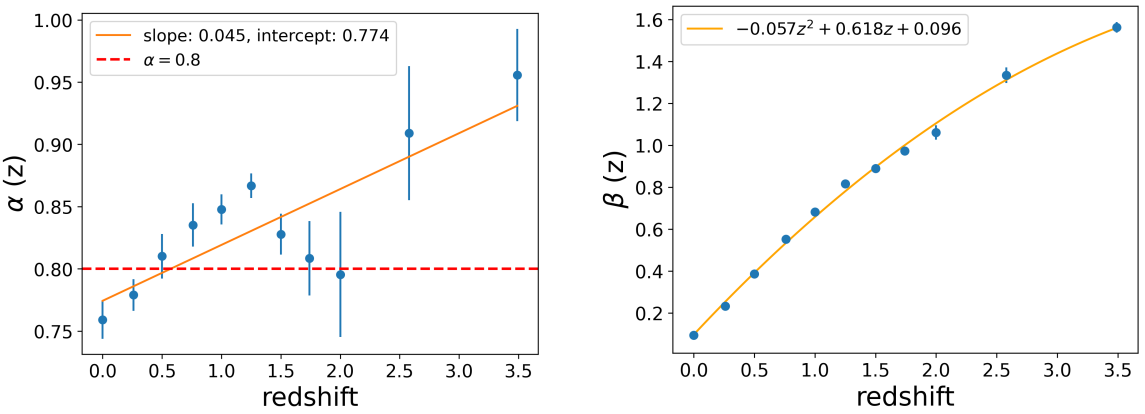

Figure 2.6: The slope (left) and intercept (right) of the SFMS in TNG100 as functions of redshift, using SFR averaged over the past 200 Myr. Error bars represent the square roots of the covariances of the slope and intercept at each redshift. The orange lines show the best fit trends. Due to large uncertainties in the slope at z $\geq$ 2, we adopt a fixed value $\alpha\,(z) = 0.8$ (red dashed line) across all redshifts.

2.3.3 Galaxy Morphology

Kinematic Morphology

In observational studies, galaxy morphologies are commonly determined by fitting surface brightness profiles or through visual classification (see Section 1.1.2). In simulations, the full three-dimensional kinematics of stellar particles, including their velocities and angular momenta, are directly accessible. This enables the kinematic decomposition of galaxy structures. Stellar particles with random motion and coherent rotation dominate bulges and disks, respectively (Abadi et al., 2003).

A commonly used parameter in kinematic decomposition is the stellar circularity, defined as $\epsilon = \frac{J_z}{J(E)}$, where J_z is the specific angular momentum of a stellar particle along the galaxy's rotation axis, and $J(E)$ is the maximum specific angular momentum a particle can have at its binding energy E. Particles with $\epsilon < 0$ are counter-rotating and are typically associated with the bulge, while those with $\epsilon > 0.7$

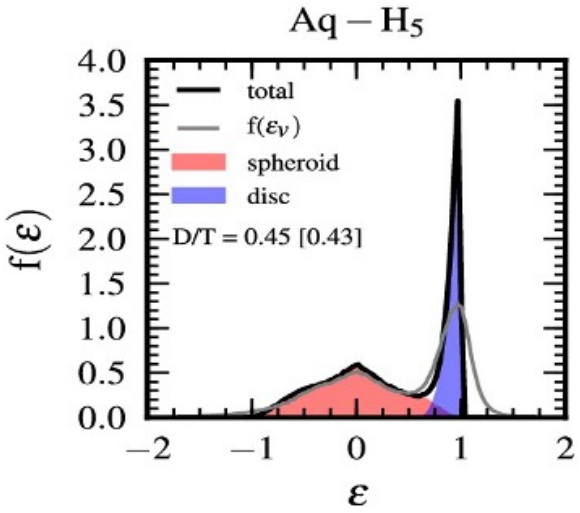

Figure 2.7: Stellar kinematic decomposition of a simulated disc galaxy. The black line shows the circularity distribution of all stellar components, while the gray line represents an alternative definition of circularity not used in this thesis. Half of the bulge mass consists of stellar particles with negative circularity. The first disc-to-total mass ratio (D/T) is calculated by subtracting the bulge mass (red) from the total stellar mass, and the second is calculated by summing all disc stellar particles (blue). Image credit: Marinacci et al. (2014)

are considered rotationally supported and make up the majority of the disk (Figure 2.7; Abadi et al. 2003; Marinacci et al. 2014; Genel et al. 2015).

In this work, we quantify the bulge-to-total stellar mass ratio (B/T) using two metrics. The first, $B/T_{\epsilon<0}$, is defined as twice the fraction of stellar mass with $\epsilon < 0$, capturing the contribution of counter-rotating stars. The second, $B/T_{\epsilon<0.7}$, is defined as the fraction of stellar mass with $\epsilon < 0.7$, which measure the contribution of stars that are not rotationally supported. Both metrics are provided in the TNG supplemental catalogs, following the method of Genel et al. (2015), and are available for all redshifts. Galaxies with $B/T_{\epsilon<0} \geq 0.6$ or $B/T_{\epsilon<0.7} \geq 0.7$ are classified as early-type. The distributions of the two B/T ratios are shown in Figure 2.8. In general, both low- and high-mass galaxies tend to be more bulge-dominated than intermediate-mass

galaxies. Low-mass galaxies, however, show a wide range of $B/T_{\epsilon<0.7}$.

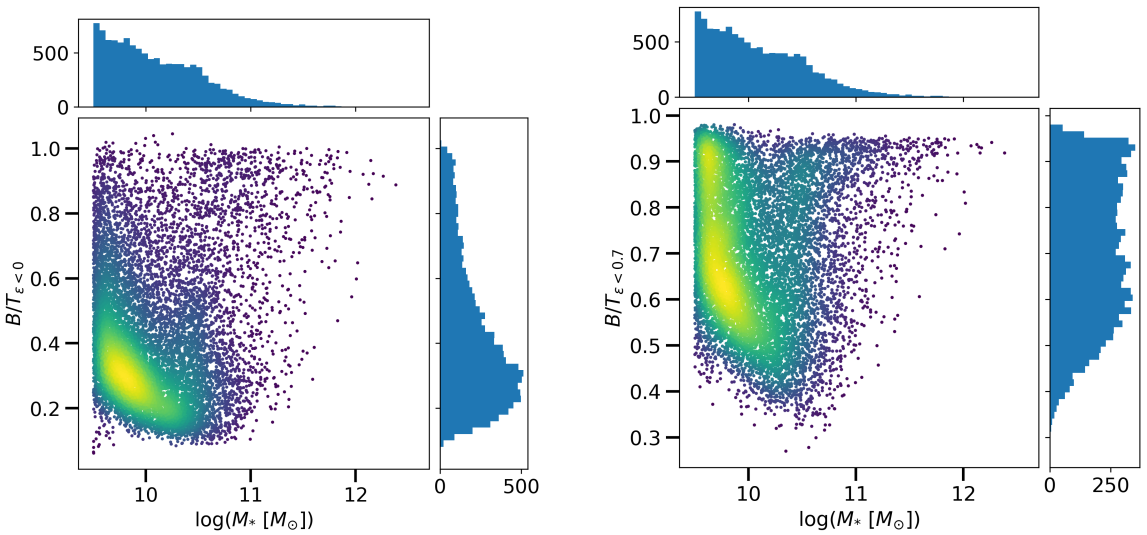

Figure 2.8: Bulge-to-total mass ratios as a function of stellar mass for TNG galaxies, based on stellar particles with $\epsilon < 0$ (left) and $\epsilon < 0.7$ (right).

Surface Brightness Morphology and Machine Learning Visual Morphology

Although kinematic morphology represents the true dynamics of the stellar components, it cannot be directly measured through observations. Moreover, several studies have shown significant discrepancies between kinematic and photometric morphologies (Jang et al., 2023; Scannapieco et al., 2010). To better match with the observational results of O24, we use two supplementary morphology catalogs designed to mimic observational classifications, based on two sets of synthetic mock images of galaxies with total stellar mass $\geq 10^{9.5}$ $M_\odot$ at z = 0, created to match SDSS observations. Dust attenuation and scattering are modeled only for galaxies with a star-forming gas-to-baryonic mass ratio greater than 1% (see Rodriguez-Gomez et al. 2019 for full details).

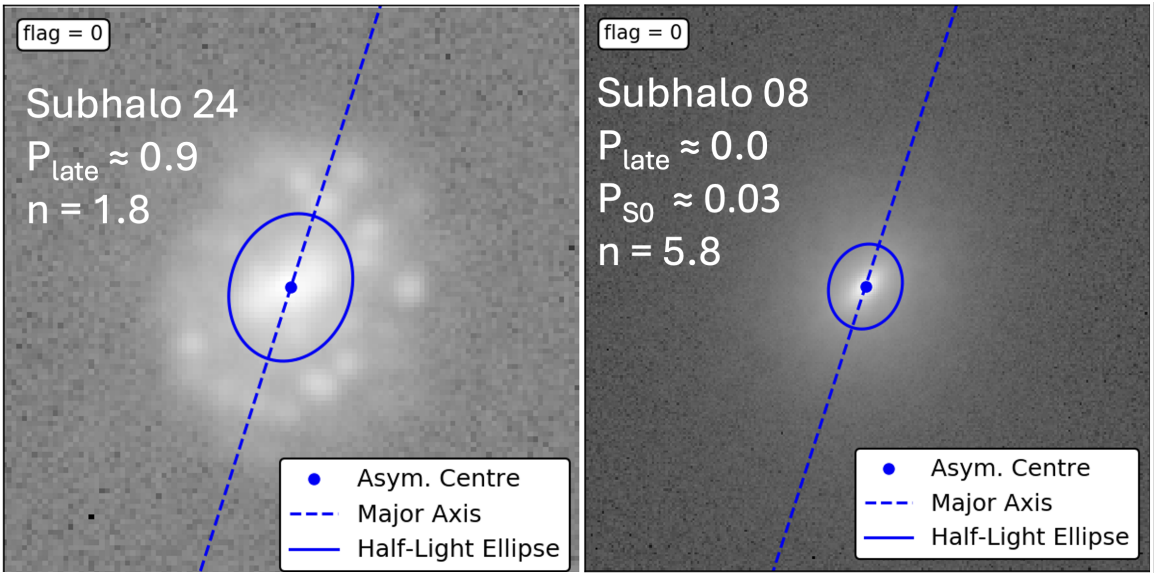

Figure 2.9: Mock stellar light images of two example galaxies in TNG100 at z = 0 created by Rodriguez-Gomez et al. (2019). Late-type galaxy (left) and elliptical galaxy (right). The Sérsic index is measured within the blue ellipse.

First, we use the i-band Sérsic index measured by Rodriguez-Gomez et al. (2019), obtained using elliptical apertures (see Figure 2.9). We include only galaxies with flag = 0 in both the morphological measurement and the Sérsic fit, meaning no issues were reported during the measurement or profile fitting, and with $S/N > 2.5$. We define early-type galaxies as those with n $\geq$ 3. We note that this threshold is somewhat arbitrary; however, varying the threshold does not affect our results or conclusions, as discussed in Section 3.2.

We also use the morphology catalog by Huertas-Company et al. (2019), which employs a machine learning algorithm to classify visual morphologies based on r-band synthetic images generated following the procedures of Rodriguez-Gomez et al. (2019). In this catalog, galaxies are divided into four types: ellipticals (E), which are bulge-dominated; lenticulars (S0), which are also bulge-dominated but with a

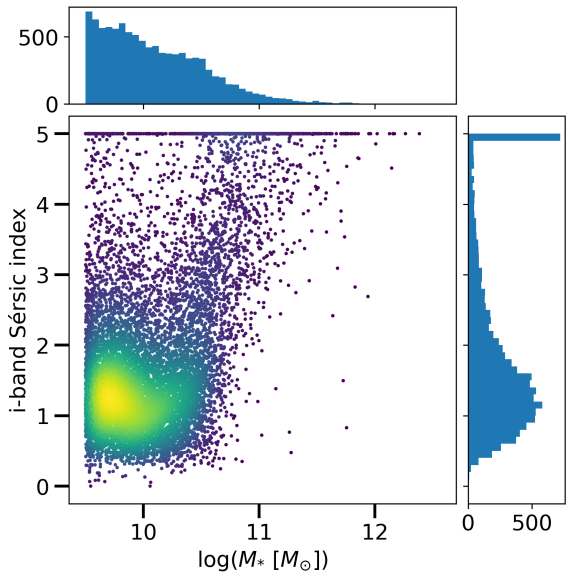

Figure 2.10: i-band Sérsic indices, measured by Rodriguez-Gomez et al. (2019) on a set of mock images, as a function of galaxy stellar mass in TNG100-1. Galaxies with Sérsic index > 5 are assigned a value of 5.

noticeable disk; early-type spirals (Sab), characterized by a small bulge and well-defined disk structures; and late-type spirals (Scd), where the bulge is minimal or negligible. Each galaxy is assigned a probability of being a late-type (P_{late}), with further subclassification: galaxies with $P_{late} > 0.5$ are assigned a probability of being Sab (P_{ab}), while those with $P_{late} \leq 0.5$ are assigned a probability of being S0 (P_{S0}). In this work, we broadly classify early-type galaxies as those with $P_{late} \leq 0.4$. We can only use these metrics when comparing with low-redshift SDSS galaxies (see Section 3.2) because they have only been measured at z = 0 and z = 0.05.

2.4 True Infall Time

We define the true infall time $T_{\rm inf,true}$ as the time since a galaxy was first classified as a member of its z = 0 host halo. $T_{\rm sat}$ denotes the time since a galaxy was classified as a satellite. The time spent in other halos prior to infall into their final host, known as the preprocessing time, is then defined as $T_{\rm prep} = T_{\rm sat}$ - $T_{\rm inf,true}$, galaxies with $T_{\rm prep}$= 0 are considered first infallers. The schematic infall timeline of a galaxy that undergoes pre-processing is shown in Figure 2.11. The SUBFIND algorithm sometimes has fluctuations in galaxy host classification across simulation snapshots. To address this, we apply a one-dimensional median filter with a window size of five snapshots to the classification time series. For each snapshot, the classification is replaced by the median value within the surrounding window to smooth out the fluctuations.[1] Following median filtering, we correct short ($\leq$ 2 snapshots) fluctuations in a galaxy's classification by setting them to match the surrounding values. This removes temporary switches between central and satellite status or brief changes in host halo assignment.

2.5 Sample Selection

We focus on the evolution of galaxies with stellar masses greater than 10^9 $M_\odot$, ensuring that each galaxy is well-resolved with more than 1000 stellar particles. Subhalos flagged as having formed within an existing halo or likely fragments of galactic structures are removed [2]. We cross-match our sample with the SFR (see Section 2.3.1)

[1] For each satellite, we define a binary infall history where a value of 1 denotes that the galaxy is within its final host halo at a given snapshot, and 0 indicates it is outside.

[2] That is, subhalos with "SubhaloFlag" set to zero in the IllustrisTNG group catalog.

and kinematic morphology catalogs (Section 2.3.3), as well as with the main progenitor branch, which traces the primary evolutionary history of each galaxy across simulation snapshots.

Satellite Galaxies

We focus on satellites that remain within their final host halo from the time of infall until z = 0, excluding backsplash galaxies, which have left the halo temporarily and do not experience continuous host influence (e.g. Levis et al., 2025). For comparison with O24 in Section 3.1, we further cross-match our sample with the two optical morphology catalogs and select satellites located within the desired phase-space regions (see Section 2.6).

Control Central Galaxies

To distinguish environmental effects from secular evolution when studying galaxy evolution after infall (Section 3.3), each satellite is paired with a central galaxy matched in stellar mass (within 0.1 dex) at the moment of infall. All matched central galaxies must remain centrals until z = 0. We then compare their evolution over the same time interval as their corresponding satellites, from infall to z = 0. Similarly, to study the impact of pre-processing (Section 4.3), satellites that experience pre-processing ($T_{\rm prep} \neq 0$) are assigned an additional mass-matched central at the time they first became satellites (see Figure 2.11).

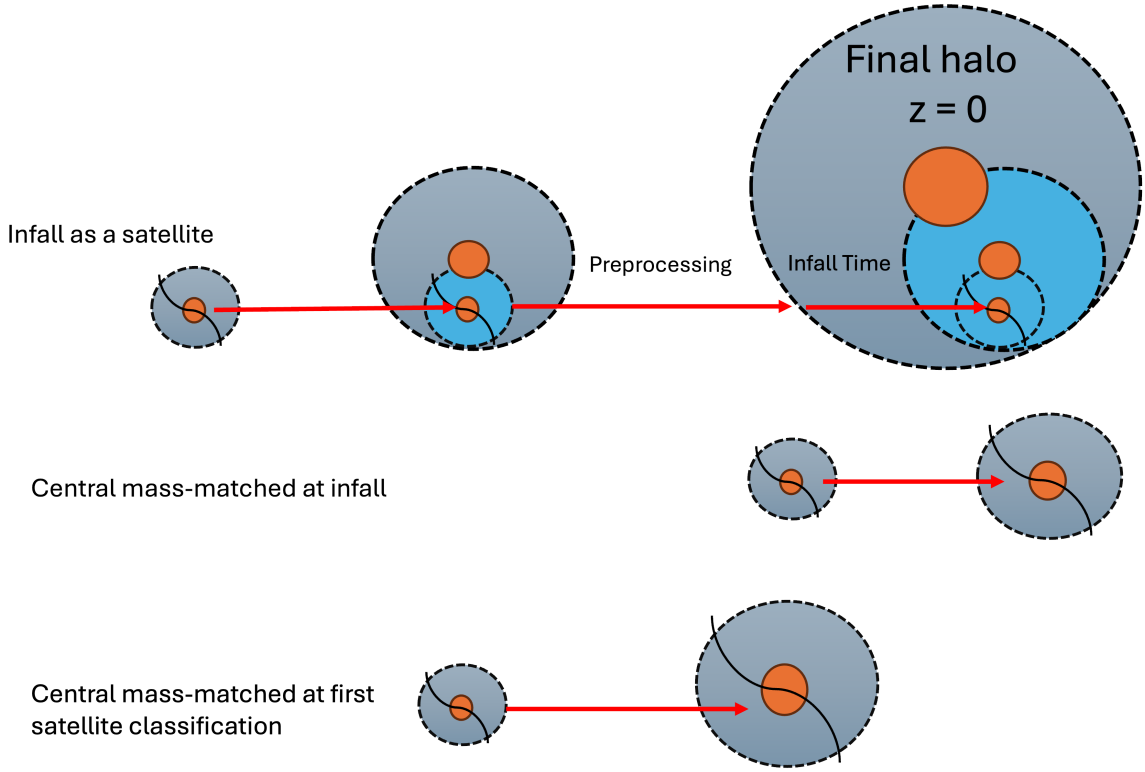

Figure 2.11: Schematic illustration of a galaxy infalling into its final halo as a satellite of another subgroup, along with the two control central samples used in this work. Centrals are shown in grey and satellites in blue. The first control set is matched to the stellar mass of satellites at the time of infall. The second set is matched to the stellar mass at the moment when galaxies are first classified as satellites. For first-infallers, these two definitions coincide. These control samples allow us to isolate the effects of environment.

2.6 Projected Phase Space Infall Time

In observational studies, there is no direct way to measure a galaxy's infall time. However, it can be estimated from a galaxy's location in the projected phase space (PPS), which shows the line-of-sight velocity (v_{LOS}) and projected distance from the cluster/group center (R_{Proj}; Figure 2.12). The x- and y-axes are normalized by the halo's virial radius (R_{200}) and velocity dispersion (σ_{LOS}), respectively. N-body simulations show that galaxies follow well-defined trajectories during infall (see the black trajectory in the left panel of Figure 2.12; Pasquali et al. 2019; Rhee et al. 2020).

Using a zoom-in cluster simulation, Pasquali et al. (2019) focused on regions of PPS within $|v_z/\sigma_{LOS}| \leq 3$ and $R_{proj}/R_{200} \leq 1$ to minimize contamination from interlopers. Outside this region, more than 40% of the population consists of interlopers. They divided this region into eight zones, each associated with a characteristic mean infall time, defined as the time since a galaxy first crossed the virial radius of its z = 0 host halo.

For consistency, we adopt the definition of infall time from O24, which combines zones 7 and 8 of Pasquali et al. (2019) into a single region due to the narrow extent of zone 7. This merged zone is assigned a mean infall time of 1.83 Gyr. The mean infall times and corresponding standard deviations for all zones are listed in Table 2.2. We compute R_{200} and σ_{LOS} following the definitions by Yang et al. (2007):

$$\sigma_{LOS} = 379.9\ km/s\ \left(\frac{M_{halo}}{10^{14}h^{-1}M_{\odot}}\right)^{0.3214} \tag{2.6.1}$$

Zone	N	$T_{inf,PPS}$ [Gyr]	$\sigma(T_{inf,PPS})$ [Gyr]
1	200	5.42	2.51
2	272	5.18	2.60
3	283	4.50	2.57
4	329	3.89	2.34
5	149	3.36	2.36
6	60	2.77	2.29
7	117	1.83	2.47

Table 2.2: Number of satellites, mean infall time, and standard deviation of each PPS zone adopted from O24.

$$R_{200} = 1.26h^{-1}\ Mpc\ \left(\frac{M_{halo}}{10^{14}h^{-1}M_{\odot}}\right)^{\frac{1}{3}}(1+z_{group})^{-1} \tag{2.6.2}$$

where M_{halo} is the halo mass enclosed within R_{200} and z_{group} is the redshift of the group or cluster.

To mimic projection effects, we extract TNG galaxy positions only in the x-y plane and velocities along the z-axis at z = 0. We then construct the PPS by computing each satellite's projected radial distance and velocity relative to the central galaxy of its FoF host halo. We refer to this infall time as the PPS infall time ($T_{inf,PPS}$) throughout this thesis, and it is used only in Sections 3.1 and 3.2. We identify 2043 satellites with stellar mass $9 \leq \log(\mathrm{M}_{\star}/\mathrm{M}_{\odot}) < 11.5$ that meet the criteria outlined in Section 2.5 and lie within $|v_z/\sigma_{LOS}| \leq 3$ and $R_{proj}/R_{200} \leq 1$. Among these, 741 reside in clusters and 1302 in groups.

These observationally accessible SFRs, morphologies, and PPS-based infall times provide a robust basis for comparing simulated galaxies to observations, and the stellar kinematic and temporal information from TNG allows us to examine in detail how galaxy properties evolve after infall in Chapter 3.

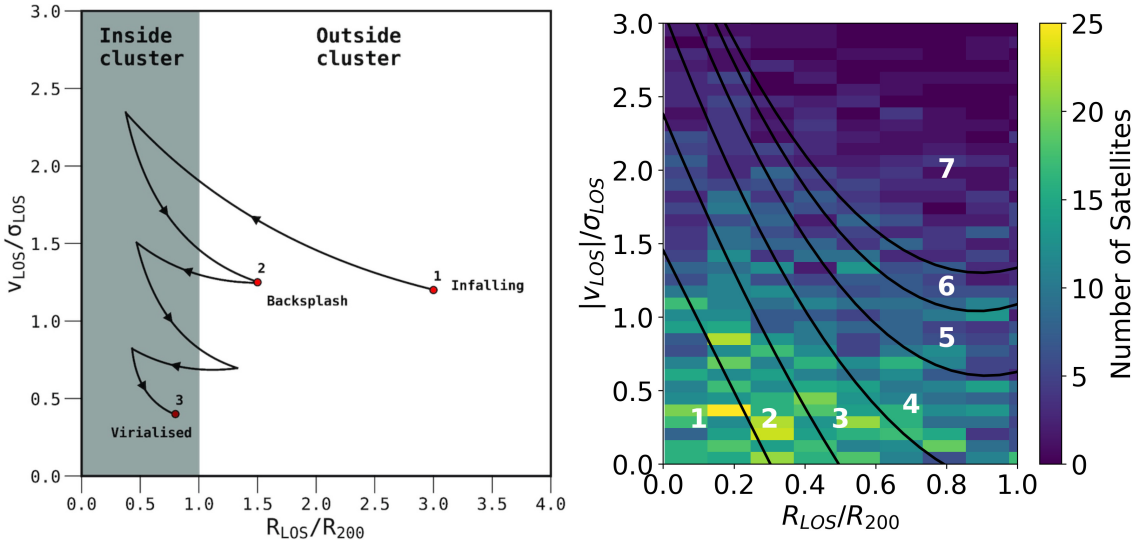

Figure 2.12: Projected phase-space (PPS) diagrams. The x- and y-axes in both panels are normalized by the halo's virial radius (R_{200}) and velocity dispersion (σ_{LOS}), respectively. Left: PPS adapted from Arthur et al. (2019). A galaxy's infall time can be estimated from its position in PPS, as it follows the black trajectory during infall. Right: PPS of the group and cluster satellites used in Sections 3.1 and 3.2, colour-coded by galaxy count. The numbers indicate the seven zones defined by Pasquali et al. (2019), with the corresponding infall times listed in Table 2.2.

Chapter 3

Results

In this chapter, we study how galaxy properties in TNG100-1 depend on infall time. In Sections 3.1 we explore how the quenched fraction of satellites at z = 0 depends on different definitions of infall time, and we compare these trends with SDSS observations from Oxland et al. (2024). Similarly, in Section 3.2 we examine the early-type fraction using four different morphology classification schemes. In Section 3.3, we extend our analysis by examining satellite properties at infall and how their star formation activity and morphology evolve afterward.

3.1 Quenched Fraction

Figure 3.1 shows the quenched fraction (QF) as a function of $T_{\rm inf,true}$ and $T_{\rm inf,PPS}$, where QF is defined as the fraction of galaxies with $\log(\text{sSFR } [\text{yr}^{-1}]) < -11$ at z = 0 within each time bin. This threshold is consistent with O24, which approximately corresponds to the local minimum of the bimodal sSFR distribution. For trends based on true infall time ($T_{\rm inf,true}$), defined as the time since a galaxy first became

a member of its z = 0 host halo, galaxies with $T_{\rm inf,true}$ less than 8 Gyr are divided into six equal-width bins, while those with $T_{\rm inf,true} > 8$ Gyr are grouped into a single bin. Each data point represents the median $T_{\rm inf,true}$ of the corresponding bin. All bins contain more than 15 galaxies, except for the $T_{\rm inf,true} \sim 1$ Gyr bin in the high-mass range, which includes only 11 cluster galaxies. Field galaxies are assigned a value of $T_{\rm inf,PPS} = 0$. The two columns correspond to galaxies with stellar masses of $9.5 \leq \log(\mathrm{M}_\star/\mathrm{M}_\odot) < 10.1$ and $10.1 \leq \log(\mathrm{M}_\star/\mathrm{M}_\odot) < 11.5$ at z = 0.

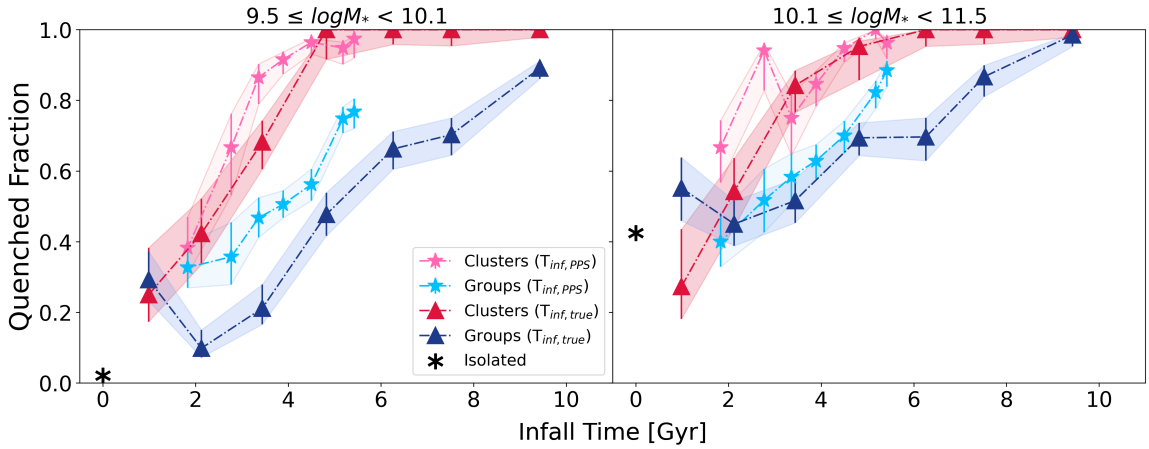

Figure 3.1: Quenched fraction as a function of true and PPS infall times. Panels are separated by galaxy stellar mass at z = 0. Trends based on $T_{\rm inf,PPS}$ and $T_{\rm inf,true}$ are shown with stars and triangles, respectively. Redder colours correspond to galaxies residing in clusters at z = 0, while bluer colours represent galaxies in groups. Black stars indicate the fraction of quenched field galaxies. Error bars represent 68% confidence intervals, calculated using the beta distribution method of Cameron (2011). In general, QF increases with infall times, and the trends based on $T_{\rm inf,PPS}$ and $T_{\rm inf,true}$ are broadly consistent within their overlapping time range.

The QF increases with $T_{\rm inf,true}$ across both environments, with cluster satellites showing a steeper slope than those in groups. In general, low-mass satellites show stronger trends than high-mass satellites within the same environment, indicating that they are more susceptible to environmental effects. It is worth noting that the

QF in groups slightly decreases ~ 2 Gyr after infall before rising again, whereas the QF of cluster satellites increases steadily with infall time.

Although in groups $T_{\rm inf,PPS}$ slightly overestimates the QF of low-mass satellites, the QF trends based on $T_{\rm inf,true}$ and $T_{\rm inf,PPS}$ are surprisingly similar within the overlapping time range, indicating that the infall times estimated by the PPS method are reasonably reliable for capturing the overall infalling behavior.

In addition to SFR, we also classify quenched galaxies using rest-frame U, V, and J-band magnitudes at z = 0, measured from mock images in Gebek et al. (2024). The resulting trends are consistent with those based on SFR. Detailed methodology and results are provided in Appendix B.

Quenched Fraction Comparison Between TNG and SDSS at Low Redshift

Figure 3.2 compares quenched fractions in TNG and SDSS as a function of PPS-inferred infall time for galaxies with $9.5 \leq \log(\mathrm{M}_\star/\mathrm{M}_\odot) < 10.4$ at low-redshift. O24 also studied galaxies with $\log(\mathrm{M}_\star/\mathrm{M}_\odot) \geq 10.4$ by dividing them into two mass bins. We restrict our comparison to their low-mass panel only due to the limited number of high-mass galaxies in TNG100.

TNG successfully reproduces the observed SDSS trend of increasing QF with $T_{\rm inf,PPS}$, including the steepest trend observed in cluster environments. The QF of field galaxies in TNG also agrees well with SDSS observations. However, TNG significantly overpredicts the QF in both clusters and groups, with the discrepancy between TNG and SDSS increasing with $T_{\rm inf,PPS}$, clearly indicating that environmental quenching in TNG is too strong.

Donnari et al. (2021b) showed that the quenched fraction (QF) of low-redshift

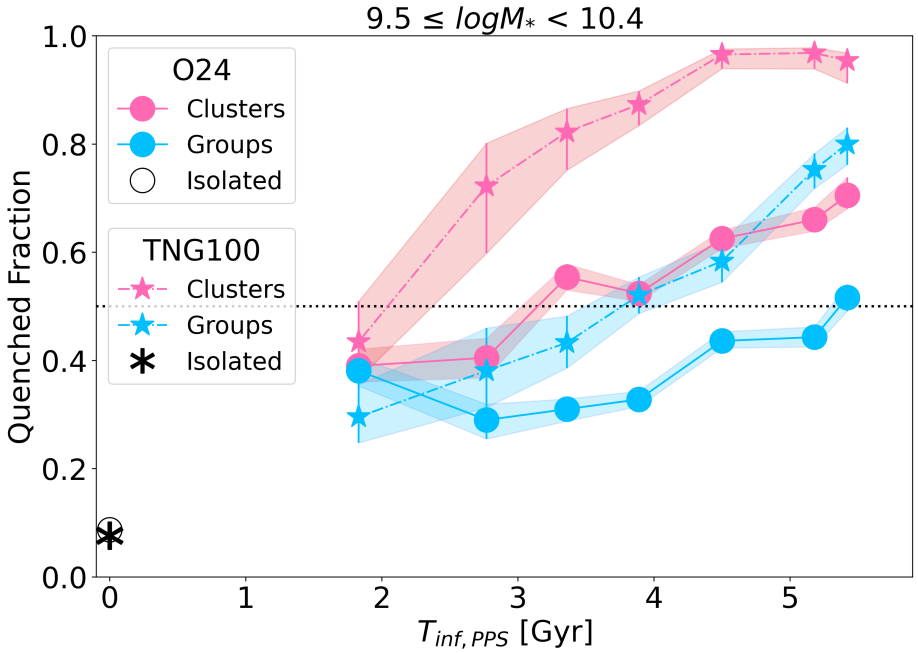

Figure 3.2: QF as a function of PPS infall time for galaxies in TNG (stars) and SDSS (circles; O24, Oxland et al. 2024). Colours and error bar calculations are the same as those in Figure 3.1. The dotted line indicated where half of the galaxies are early-type. TNG reproduces the observed SDSS trend of increasing QF with PPS infall time and matches the field QF, but it overpredicts the QF in high-density environments.

centrals with $9.5 \leq \log(M_\star/M_\odot) < 10$ in all three TNG volumes agrees well with SAMI and GAMA observations, in which nearly all galaxies are star forming (see Figure 2.4). In contrast, they found that the QF of cluster satellites with $9.7 \leq M_\star < 10.5$ in TNG300 is higher than in SDSS observations by roughly 20% at any projected clustercentric distance (see their Figure 9). Our results are consistent with theirs and extend the analysis by showing that the largest discrepancy occurs in the inner region of the phase-space diagram. These findings suggest that the gas stripping and/or feedback models implemented in TNG may quench satellites too efficiently. This topic is discussed in more detail in Section 4.1.

Interlopers

Another common observational challenge is contamination from interlopers, field galaxies that appear to be satellites due to projection. To mimic this effect, for each cluster and group, field galaxies that lie within $|v_z/\sigma_{LOS}| \leq 3$ and $R_{proj}/R_{200} \leq 1$ are considered interlopers and reclassified as satellites of that halo and removed from our field sample. Table 3.1 presents the total number of galaxies in each PPS zone after including interlopers, along with the interloper fraction per region.

Zone	$N_{Sat+Intl}$	Interloper	f_{intl}
1	204	4	0.020
2	273	1	0.0037
3	299	16	0.054
4	364	35	0.096
5	165	16	0.097
6	67	7	0.10
7	134	17	0.13

Table 3.1: Total number of satellites and interlopers, number of interlopers, and interloper fraction in each PPS region.

The QF trend including interlopers is shown in Figure A.3. Even when interlopers are considered, TNG still overestimates the QF compared to SDSS. In fact, Table 3.1 shows that the interloper fraction decreases toward the inner PPS regions, in agreement with the findings of Pasquali et al. (2019). However, our analysis shows that the discrepancy with SDSS becomes more pronounced in the central zones (longer infall time). This suggests that contamination from interlopers alone cannot explain the observed differences between TNG and SDSS.

3.2 Early-type Fraction

Having established how star formation is suppressed after infall, we now examine whether morphology evolves on similar timescales. Figure 3.3 shows the early-type fraction (EF) as a function of $T_{\rm inf,true}$, based on four morphological definitions of early-type galaxies introduced in Section 2.3.3: (a) $B/T_{\epsilon<0} \geq 0.6$, (b) $B/T_{\epsilon<0.7} \geq 0.7$, (c) Sérsic index ≥ 3, and (d) $\mathrm{P}_{late} \leq 0.4$. Each definition corresponds to a separate row in the figure.

Among the four indicators, the EF based on $B/T_{\epsilon<0.7}$ (panel b) shows an increasing trend with infall time and is higher in denser environments in both mass bins. The visual morphology classification (panel d) shows a similar trend, but only within the high-mass bin. In contrast, the EFs based on $B/T_{\epsilon<0}$ (panel a) and Sérsic index (panel c) show much weaker trends and remains relatively constant across environments. Notably, the Sérsic index-based EF even decreases with infall time in the high-mass bin. We tested alternative Sérsic thresholds and found that the overall trends with $T_{\rm inf,true}$ remain fairly unchanged (see Figure A.4).

For completeness, Figure A.5 shows the median values of each indicator as a function of $T_{\rm inf,true}$. These trends are broadly similar to those in Figure 3.3, and show only weak dependence on $T_{\rm inf,true}$ and environment, except for P_{late}. In fact, the four indicators yield substantially different EF values, suggesting an inconsistency between them. We further discuss this in Section 4.2.

Early-Type Fraction Comparison Between TNG and SDSS at Low Redshift

Figure 3.4 compares the EFs as a function of $T_{\rm inf,PPS}$ between TNG and the observational results from O24, using four morphology indicators. With the exception of

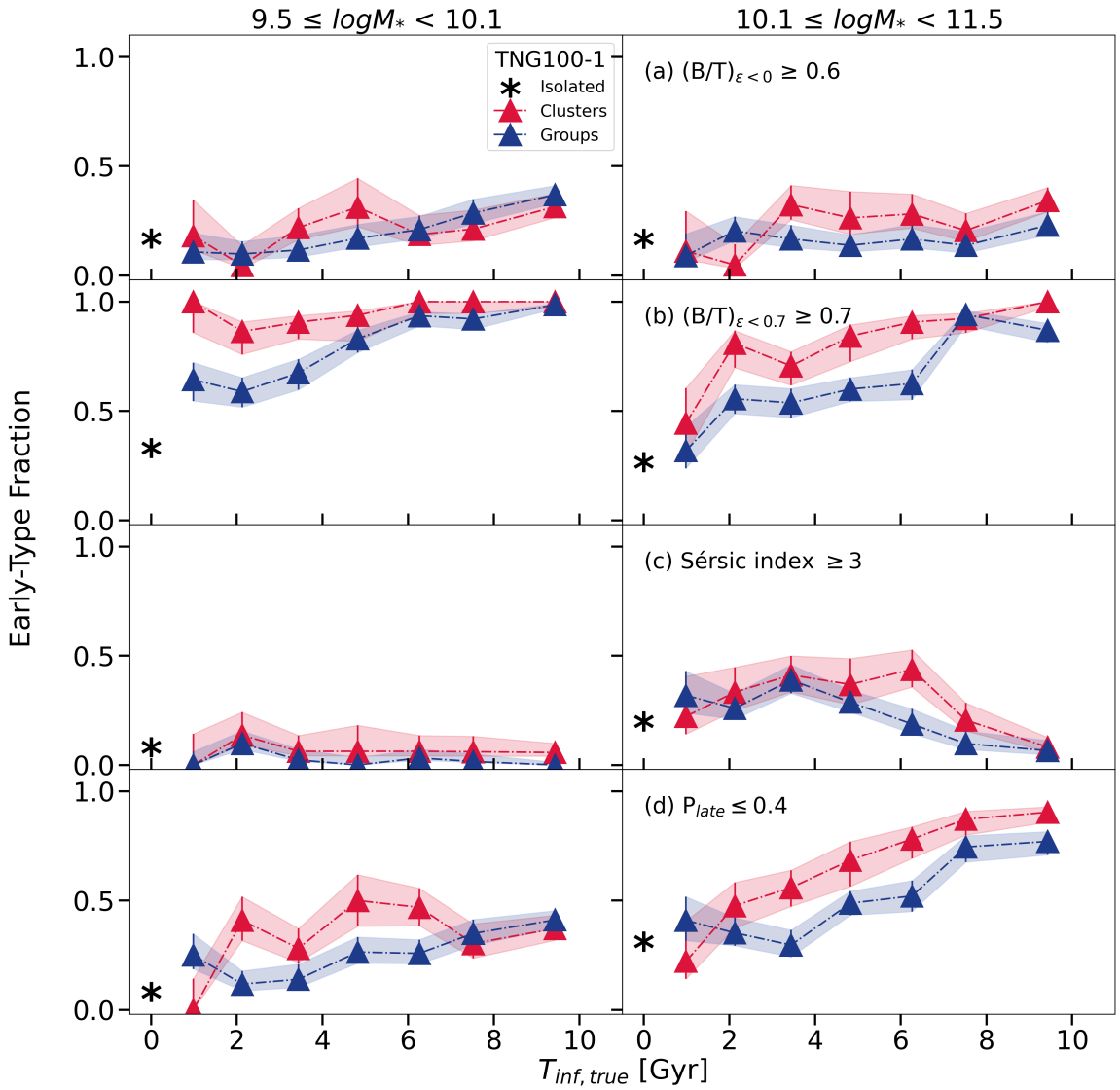

Figure 3.3: Early-type fractions as a function of true infall time using four different morphology indicators. Early-type galaxies in each row are defined as follows: (a) $B/T_{\epsilon<0} \geq$ 0.6; (b) $B/T_{\epsilon<0.7} \geq$ 0.7; (c) Sérsic index $\geq$ 3; (d) $P_{late} \leq$ 0.4. The two columns, colour schemes, and error bar calculations are the same as in Figure 3.3, except that $T_{\rm inf,PPS}$ trends are not shown. Overall, EF trends vary among the four indicators: panels (b) and (d) show an increasing trend with infall time, while panels (a) and (c) do not.

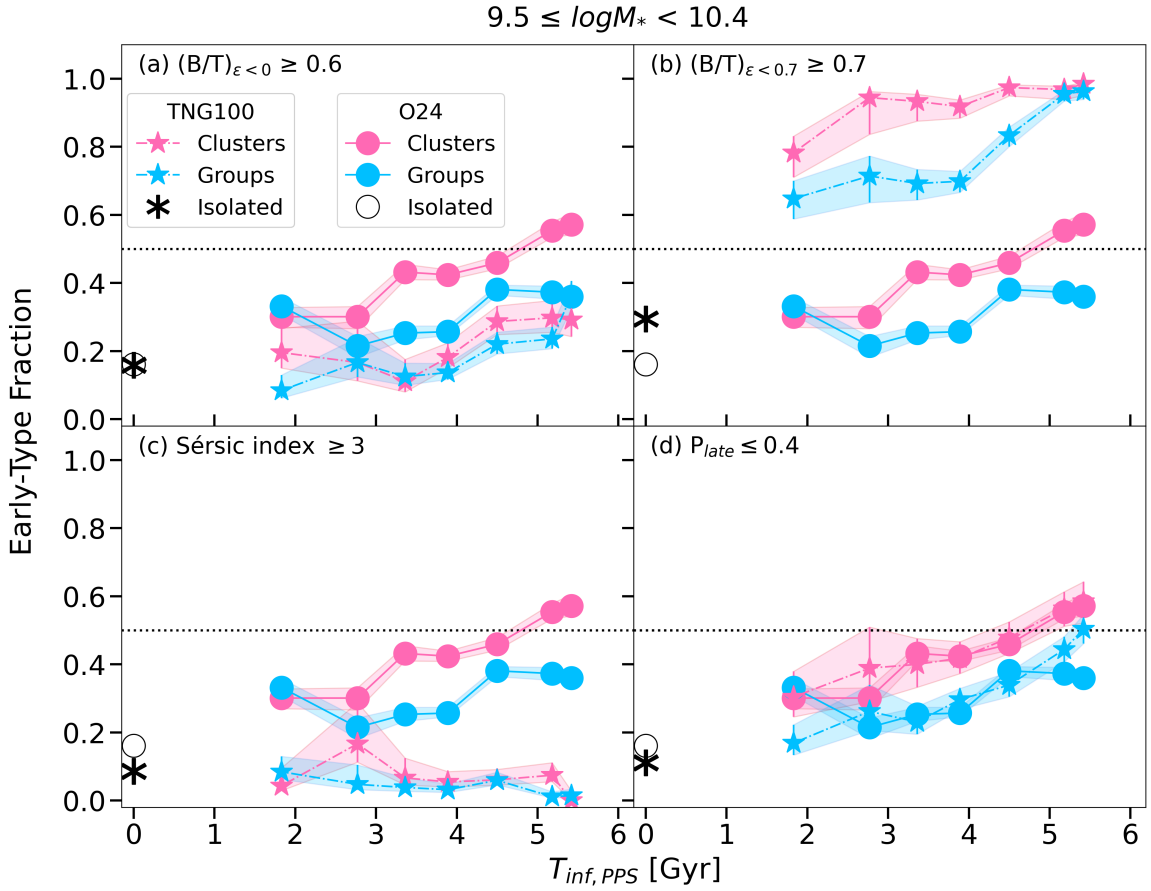

Figure 3.4: EFs as a function of PPS infall time for galaxies in TNG (stars) and SDSS (circles), using four morphology indicators. Colours and error bar calculations are the same as those in Figure 3.1. The dotted line indicated where half of the galaxies are early-type. TNG reproduces the observed SDSS result of no strong trend with infall time (except for panel (c)) and matches the EF of field population.

of the trend based on Sérsic index [1], the other three indicators reproduce the observed weak dependence of EF on infall time and environment. Additionally, all four indicators roughly match the EF of the field populations.

3.3 Evolution of Galaxy Properties in TNG After Infall

In Sections 3.1 and 3.2, we discussed how the fractions of quenched and early-type satellites at z = 0 depend on infall time, using galaxy morphology and star formation rate measured at z = 0. Here, we extend this analysis by comparing galaxy star formation and morphology at the time of infall with their properties at z = 0, as a function of true infall time, to study how these properties evolve during infall into their host halos.

In this section, we no longer restrict the sample to satellites included in the two mock-image-based morphology catalogs described in Section 2.3.3, as these catalogs are not available at all redshifts. We also remove the selection criteria of $|v_z/\sigma_{LOS}| \leq 3$ and $R_{proj}/R_{200} \leq 1$ since we are not using PPS-inferred infall time.

Previous studies have shown that, in simulations, two-body scattering between stellar and dark matter particles, as well as between stellar particles themselves, can artificially increase stellar velocity dispersion and reduce the orbital circularity if the simulated galaxies are not well-resolved (Ludlow et al., 2021; Wilkinson et al., 2023; Ludlow et al., 2023; Zeng et al., 2024). As shown in Wilkinson et al. (2023), such numerical heating can reduce the fraction of stellar particles with circularity

[1]We also tested whether lowering the Sérsic index threshold would improve agreement with observations. However, this led to a more pronounced decreasing EF trend.

> 0.7, whereas the fraction of counter-rotating stars ($\epsilon < 0$) is much less affected (see their figures 9 and 10). Zeng et al. (2024) further suggest that stellar kinematics remain robust against numerical heating when galaxies are resolved with more than 10000 stellar particles within twice the stellar half-mass radius. At the resolution of TNG100, this corresponds to a stellar mass of approximately $10^{10}\mathrm{M}_{\odot}$. Therefore, we limit our analysis to galaxies with stellar masses in the range $10 \leq \log(\mathrm{M}_{\star}/\mathrm{M}_{\odot}) < 11.5$ at the time of infall and focus on only the evolution of $B/T_{\epsilon<0}$. For completeness, we also show the evolution of properties for galaxies with $9.5 \leq \log(\mathrm{M}_{\star}\ [\mathrm{M}_{\odot}]) < 10$ in Figure A.6.

To study the evolution of star formation activity after infall, we exclude satellites that had zero SFR at the time of infall: 151 in groups (22% of group satellites) and 111 in clusters (25% of cluster satellites). The final sample consists of 545 group satellites and 341 cluster satellites. We are interested in how the offset from the SFMS for these satellites changes after infall. The SFMS at each redshift is defined by the relation between stellar mass and SFR, using Equation 2.3.1 with a redshift-dependent slope and intercept, as described in Section 2.3.2. For each galaxy, the offset from the main sequence is calculated as the difference between its $\log(\mathrm{SFR}_{200})$ and the expected SFMS value at the same stellar mass and redshift. Galaxies with zero SFR at z = 0 are assigned a value of $\log(\mathrm{SFR}_{200}\ [\mathrm{M}_{\odot}\ \mathrm{yr}^{-1}]) = -4$ when calculating the offset from MS.

3.3.1 Star Forming Activity

Figure 3.5 shows how galaxy stellar mass, offset from the main sequence, and gas mass change after infall. Each data point represents the median change in each time

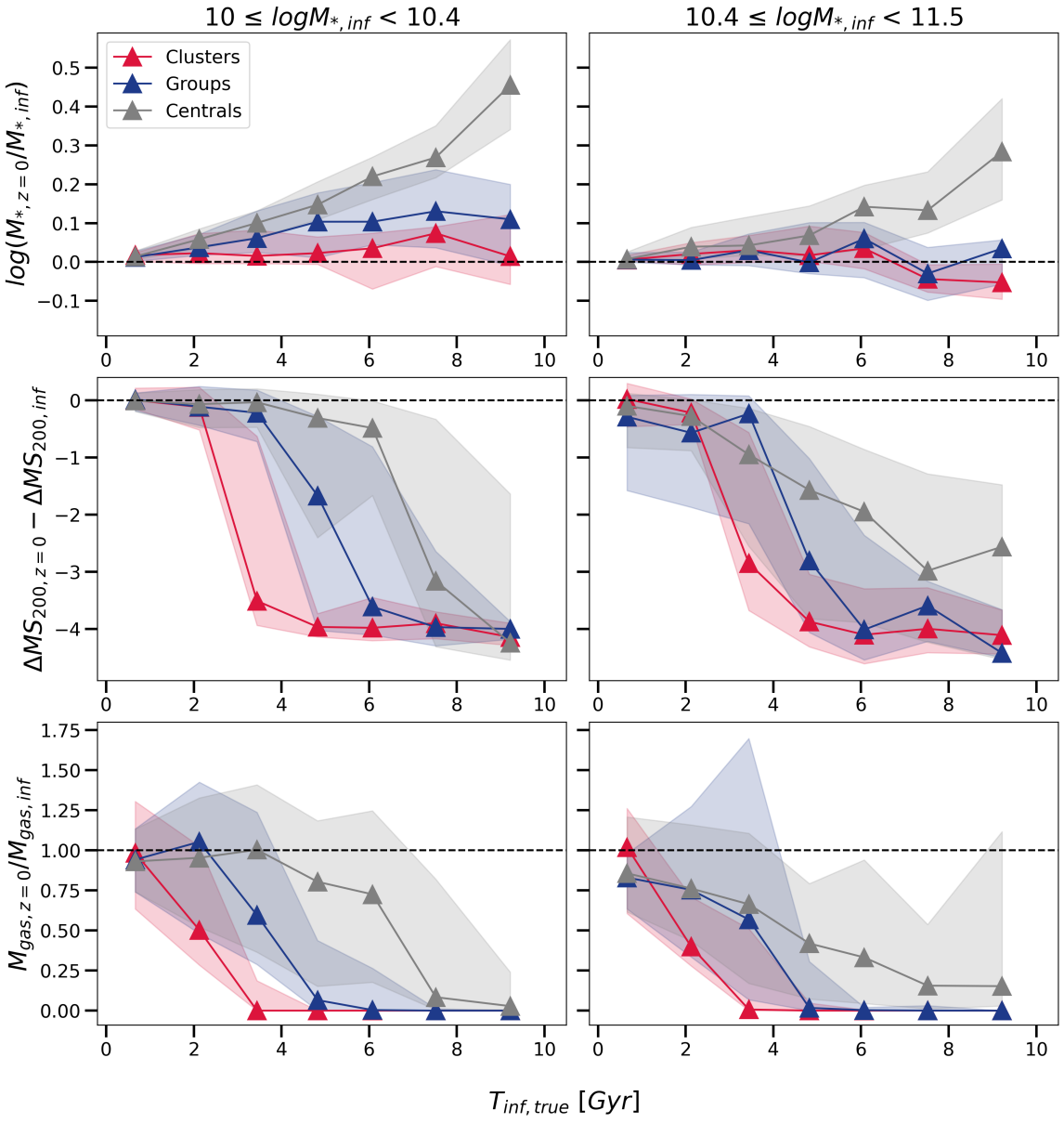

Figure 3.5: Change in galaxy stellar mass, main sequence offset, and gas mass from infall to z = 0, as a function of true infall time. Each panel displays the median trend, with shaded regions representing the 25th and 75th percentiles. Columns correspond to two stellar mass bins defined at the time of infall. Line styles for satellites follow those in Figure 3.1, while grey lines represent mass-matched central galaxies based on stellar mass at infall. The black dashed line indicates zero change.

bin. For each environment, every time bin includes at least 10 galaxies. The two columns correspond to intermediate-mass ($10 \leq \log(M_{\star,inf}/M_{\odot}) < 10.4$) and high-mass ($10.4 \leq \log(M_{\star,inf}/M_{\odot}) < 11.5$) galaxies, based on stellar mass at the time of infall. For comparison, the evolution of mass-matched centrals (see Section 2.5 for definition) over the same period is shown in grey.

Stellar Mass Growth

The top panel of Figure 3.5 shows the ratio of stellar mass at z = 0 to that at the time of infall. Values above the black dashed line indicate growth in stellar mass. Centrals grow steadily in stellar mass over time, while satellites show little to no growth after infall. This suggests that stellar mass growth is strongly suppressed for satellites after infall. In particular, high-mass satellites with long infall times (clusters: > 7 Gyr; groups: > 5 Gyr) even experience slight mass loss. Figure A.9 shows the 3D halo-centric distance of satellites at $z = 0$ as a function of $T_{\rm inf,true}$. Galaxies that have experienced mass loss are located near the halo center, likely undergoing tidal stripping by the central galaxy prior to merging (Wang et al., 2019).

Offset From Star Forming Main Sequence

We next study how the offset from the main sequence changes after infall in the second row of Figure 3.5. Both satellites and centrals tend to move below the MS over time, with centrals showing greater scatter. This indicates that galaxies generally becoming less active in star formation. Satellites, however, fall below the MS more rapidly, with timescales depending on both stellar mass and environment. Cluster satellites with infall times of roughly 1–3 Gyr are still star forming, whereas those

with infall times greater than 3 Gyr are mostly quenched. Group satellites follow a similar trend but sustain steady star formation for somewhat longer, up to ~ 4 Gyr. These results are consistent with the so-called 'delayed-then-rapid' quenching scenario (Wetzel et al., 2012; Ding et al., 2024). That is, satellites experience a period of relatively constant star formation following infall, followed by a rapid shutdown in less than 1 Gyr (Wetzel et al., 2012). For completeness, the SFR_{200} at z = 0 as a function of $T_{\mathrm{inf,true}}$ is shown in Figure A.7.

Total Gas Mass

Numerous studies have suggested that starvation and ram pressure stripping are the primary mechanisms of satellite quenching (e.g. Heß & Springel, 2012; Steinhauser et al., 2016; Rodríguez-Cardoso et al., 2025). To investigate this further, the bottom row of Figure 3.5 shows the ratio of total gas mass at z = 0 to that at infall, as a function of infall time. While both centrals and satellites lose gas over time, satellites in clusters experience the most rapid decline, followed by those in groups. For a large fraction of cluster satellites, only about 50% of their initial gas mass remains after just 2 Gyr of infall, whereas group satellites take roughly 4 Gyr to reach a similar level of gas loss. In both mass bins, some group satellites show an increase in gas mass after infall. In particular, those high mass group satellites also show a more active star formation. This may be due to ongoing minor mergers, as previously observed in certain gas-rich galaxy groups (e.g. Džudžar et al., 2019).

Taken together with the second row (see also Figure A.7), TNG satellites tend to maintain their star-forming activity even after losing up to 50% of their gas shortly after infall. They do not become quenched until all of their gas is lost. This is

consistent with previous findings that star formation in satellites shuts down rapidly once the cold ISM is removed (Cortese et al., 2021; Rohr et al., 2023).

Although Figure A.9, which shows the present-day halo-centric distance of satellites as a function of $T_{\rm inf,true}$, does not provide the exact timing or number of pericentric passages experienced by the satellites, it enables us to infer their occurrence, as galaxies typically follow a characteristic zig-zag trajectory during infall (as illustrated in the PPS diagram from Arthur et al. (2019), Figure 2.12). In our cluster sample, the first pericentric passage starts roughly 2 Gyr after infall, while in our group sample it occurs later, at about 3 Gyr. Thus, at least for our cluster satellites, they tend to quench and lose most of their gas during the first pericentric passage. Similar results have been found in TNG300 (Park et al., 2023), other simulations such as Magneticum Pathfinder (Lotz et al., 2019) and YZiCS (Jung et al., 2018), and in observations (Haines et al., 2015).

3.3.2 Kinematic Morphology

Figure 3.6 shows the change in $B/T_{\epsilon<0}$ after infall as a function of $T_{\rm inf,true}$. Overall, satellites gradually become more bulge-dominated following infall. In contrast, intermediate-mass centrals tend to become more disk-dominated over time, whereas high-mass centrals become more bulge-dominated, similar to satellites. The time at which the bulge growth of satellites begins to differ from that of centrals after infall appears to depend on stellar mass but not on environment. Intermediate-mass satellites show noticeable divergence around 3.5 Gyr after infall, while high-mass satellites remain similar to centrals until approximately 8 Gyr after infall.

In fact, as the stellar mass growth of satellites is strongly suppressed after infall

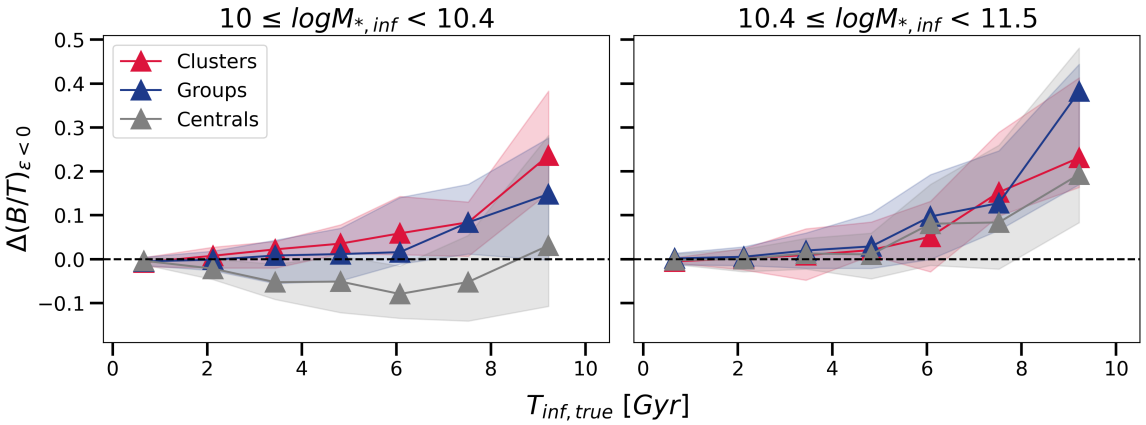

Figure 3.6: Difference in $B/T_{\epsilon<0}$ between z = 0 and infall as a function of true infall time. Panel layout and line styles follow those in Figure 3.5. Values above the dashed line indicate an increase in $B/T_{\epsilon<0}$.

(Figure 3.5), the increase in $B/T_{\epsilon<0}$ after infall indicates a genuine increase in the amount of counter-rotating stars. In contrast, the decrease in $B/T_{\epsilon<0}$ among intermediate centrals is likely due to dilution from in situ star formation. Pillepich et al. (2019) have shown that the cold dense gas in TNG galaxies is disky and rotationally supported. Newly formed stellar particles are likely to be initially rotation-supported (e.g., Joshi et al., 2020; Zeng et al., 2024). Thus, as intermediate-mass centrals experience significant stellar mass growth, in situ star formation could replenish rotation-supported stellar particles and drive the observed decrease in $B/T_{\epsilon<0}$.

We also examine the evolution of the fraction of non-rotationally supported stellar particles ($B/T_{\epsilon<0.7}$) in Figure A.8. Similar to the change in $B/T_{\epsilon<0}$, galaxies generally become more bulge-dominated over time, except for intermediate-mass centrals. However, the divergence between satellites and centrals appears at earlier infall times in $B/T_{\epsilon<0.7}$ than in $B/T_{\epsilon<0}$, and the intermediate-mass satellites show a clearer environmental dependence in $B/T_{\epsilon<0.7}$.

3.4 Quenching Prior to Morphological Transformation

Our results indicate a clear contrast between quenching and morphological transformation: quenching occurs rapidly, with strong dependence on both environment and stellar mass, whereas morphological transformation proceeds gradually and is primarily mass-dependent. More importantly, star formation ceases before significant structural changes take place, consistent with numerous observational studies. Using SDSS observations, O24 found that, at fixed stellar mass, both cluster and group satellites with $M_\star > 10^{10.4} M_\odot$ typically require ~ 5 Gyr longer for the EF to reach 0.5 than for the QF (see their Figure 5). Martínez et al. (2023) separate the satellites in SDSS into five orbital classes based on their position in the PPS, ranging from interlopers to short- and long-infall-time satellites, and use the probabilities of being elliptical (P_E) or spiral (P_S) from Galaxy Zoo (Lintott et al., 2008; Lin et al., 2023), defining elliptical as those with $P_E > P_S$. By comparing the QFs and EFs of these classes to those of interlopers, they find that the QFs for classes with longer infall times show a larger discrepancy from the interlopers than the EFs do. This supports the picture in which satellites require a longer timescale to undergo morphological transformation than to have their star formation quenched.

Overall, our results show that TNG reproduces broad trends in quenching and morphological evolution after infall, but systematic differences with SDSS observations remain. These discrepancies, along with the role of pre-processing in shaping galaxy properties and the potential mechanisms responsible for halting star formation and driving morphological transformation, are explored further in Chapter 4.

Chapter 4

Discussion

4.1 Discrepancy in Quenched Fractions Between TNG and SDSS

Our results in Chapter 3 demonstrate good agreement between TNG and SDSS for field galaxies, but show notable differences for satellites with large infall times, suggesting that the mismatch arises from parameters related to environment. Similar over-quenching for low-mass satellites relative to observations has also been reported in other simulations, such as EAGLE and Hydrangea (Bahé et al., 2017; Kukstas et al., 2020, 2023). Kukstas et al. (2023) argue that the finite resolution of these large-volume simulations may cause ram pressure stripping to be artificially efficient. Bahé et al. (2017) suggest that the stellar feedback implementation in EAGLE can cause low-mass galaxies with shallow potentials to be more extended than in the real Universe. As a result, these galaxies are more vulnerable to gas stripping after infall.

Moreover, both Heß & Springel (2012) and Steinhauser et al. (2016) show that the efficiency of gas stripping increases as the resolution of the simulation decreases, which leads to a lower star formation rate and a shorter quenching timescale. In particular, Heß & Springel (2012) found that increasing the gas cell resolution by a factor of 20 can double the time required to strip all the gas from a galaxy (see Figure 13 of their work).

Observational uncertainties can also contribute to the discrepancy. Goubert et al. (2024) argue that halo mass estimates in observations suffer from significant uncertainty (~ 0.5 dex). Moreover, O24 did not account for measurement errors in stellar mass and sSFR, which could further distort the inferred QF trends. For instance, Donnari et al. (2021b) show that adding Gaussian uncertainties of 0.2 dex to stellar mass and 0.6 dex to SFR can increase the inferred QF by roughly 10 %.

4.2 Discrepancy Between Morphology Indicators

In Section 3.2, we found that the four morphology indicators show different trends in EF vs $T_{\rm inf,PPS}$, especially when using the Sérsic index, indicating a discrepancy among the four. Figure 4.1 shows the distributions of $B/T_{\epsilon<0}$, $B/T_{\epsilon<0.7}$, and Sérsic index for spirals and early-type galaxies, based on the visual classifications by Huertas-Company et al. (2019). The agreement between kinematic and visual morphologies depends on stellar mass, with $B/T_{\epsilon<0.7}$ providing a good tracer of early-type galaxies at the high-mass end. A similar result was found by Correa et al. (2017) in the EAGLE simulation, where stellar kinetic energy effectively traced visual morphology for galaxies with $\log(\mathrm{M}_\star/\mathrm{M}_\odot) > 10$, based on a set of mock images. In contrast, the Sérsic index shows only weak correlation across both mass bins. The poor consistency

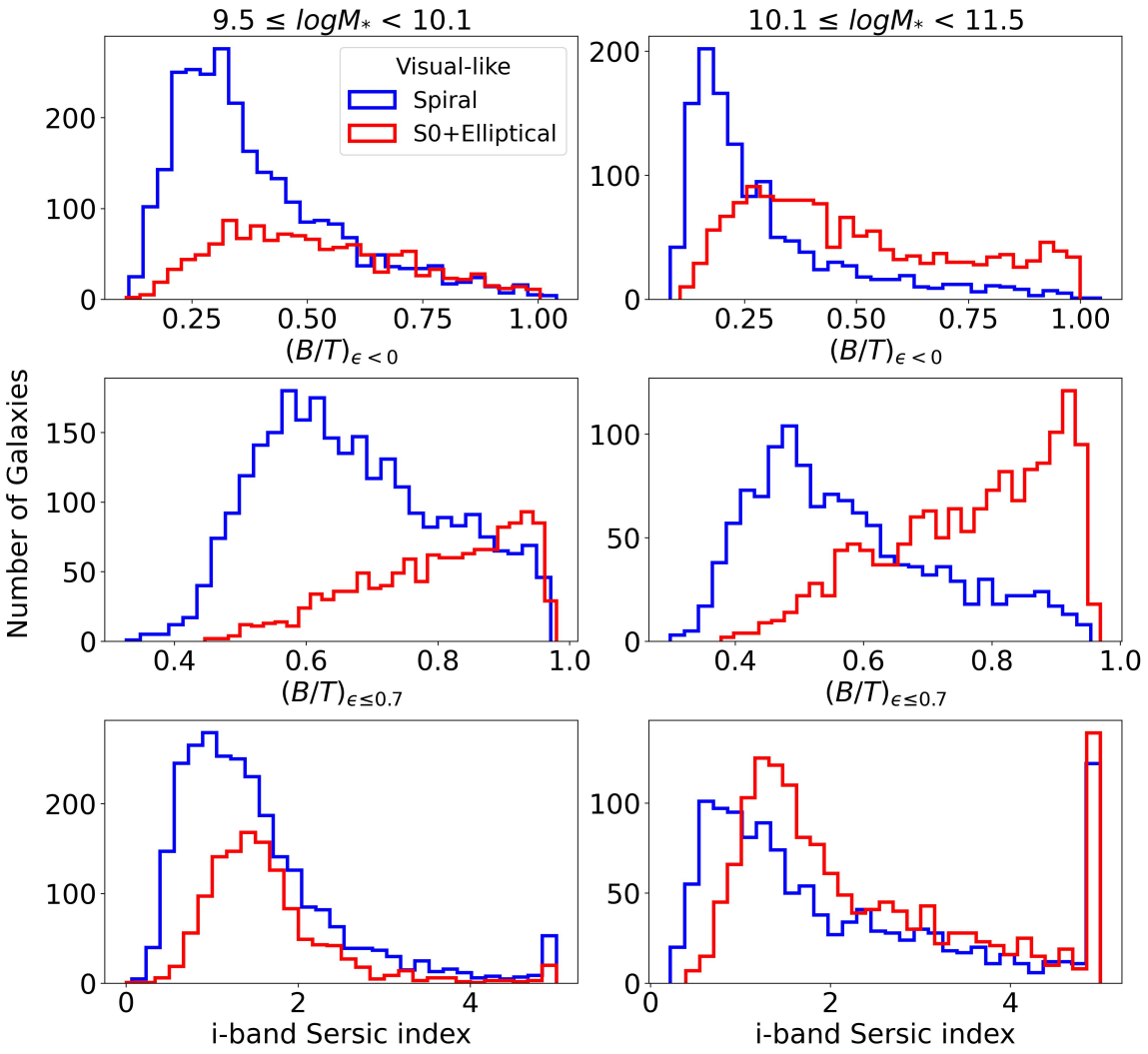

Figure 4.1: Distributions of $B/T_{\epsilon<0}$ (top), $B/T_{\epsilon<0.7}$ (middle), and Sérsic index (bottom) for spiral (blue) and early-type (red) galaxies based on the visual classification by Huertas-Company et al. (2019). Panels correspond to galaxy stellar mass at z = 0.

between Sérsic index and visual morphologies has also been reported by Huertas-Company et al. (2019).

Discrepancies between kinematic and photometric morphologies are well known in simulations. Numerous studies have shown that $B/T_{\epsilon<0}$ is generally larger than the bulge-to-total ratio from two-component Sérsic fits, particularly for galaxies with $\log(M_\star/M_\odot) \leq 10$. This trend has been observed in Illustris[1], NewHorizon[2], EAGLE, and other simulations (Scannapieco et al., 2010; Obreja et al., 2016; Bottrell et al., 2017; Thob et al., 2019; Jang et al., 2023).

The origin of these discrepancies remains unclear and requires further investigation. Possible explanations include the presence of low-mass, fast-rotator early-type galaxies in observations (Wang et al., 2020), disc fading (Kelkar et al., 2017), or numerical effects such as reduced stellar circularity due to dynamical heating in low-mass systems ($\log(M_\star/M_\odot) < 10$; Ludlow et al., 2023; Zeng et al., 2024).

4.3 Pre-processing Affects Star Formation More Than Morphology

Many satellites are not first infallers but have already spent time in smaller "sub-groups" before entering their final host halo. This pre-processing stage can remove gas and, in some cases, stellar mass well before infall, leading to shorter post-infall quenching times (Haines et al., 2015). The fraction of pre-processed galaxies and the impact of their pre-processing effects are expected to be higher in massive clusters than in groups (Donnari et al., 2021a). In this section, we study the impact of

[1]Stellar mass resolution $\sim 10^{6.1}$ $M_\odot$
[2]Stellar mass resolution $\sim 10^4$ $M_\odot$

pre-processing on galaxies prior to their infall into clusters and groups.

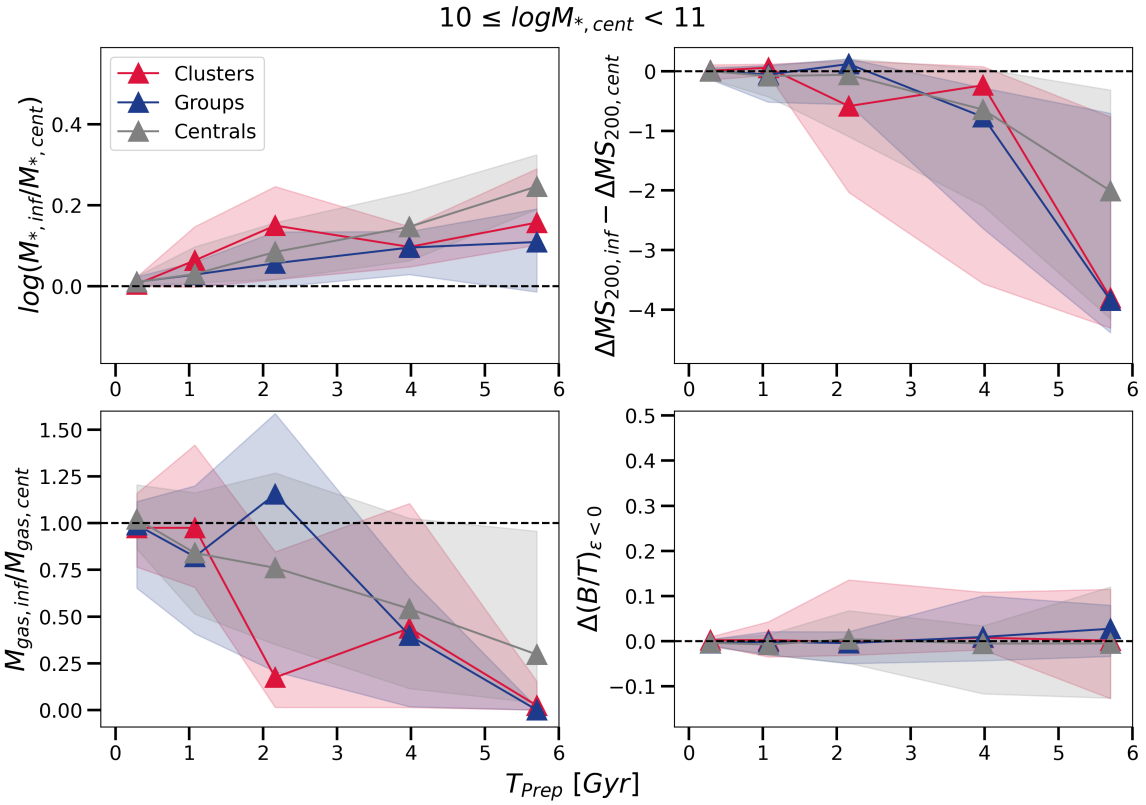

Figure 4.2: Same as Figures 3.5 and 3.6, but showing the changes between the time a galaxy is first classified as a satellite and at the moment of infall, as a function of pre-processing time.

We focus on galaxies with $T_{\rm prep} \neq 0$ that, once identified as satellites, remain satellites until $z = 0$ without ever becoming centrals again. To avoid low-number statistics for high-mass pre-processed galaxies, we restrict the study to those with stellar masses $10 \leq \log(\mathrm{M}_\star/\mathrm{M}_\odot) < 11$ at $T_{\rm sat}$. Figure 4.2 shows changes in stellar mass, offset from the main sequence, total gas mass, and $B/T_{\epsilon<0}$ between first satellite classification and the moment of infall, as a function of $T_{\rm prep}$. Control centrals are mass-matched at $T_{\rm sat}$.

We find that pre-processing has minimal impact on morphology and stellar mass

but can strongly suppress star formation and remove gas. Both cluster and group galaxies can lose over 50% of their total gas during pre-processing. Star formation in group galaxies is generally less affected, except for those with long pre-processing times, whereas cluster galaxies show significant suppression after only ~ 2 Gyr of pre-processing. Because these galaxies lose substantial gas prior to infall, they quench rapidly upon entering clusters or groups (Haines et al., 2015; Jung et al., 2018).

Our results align with previous simulations and observations, which indicate that pre-processing affects star formation and gas mass more strongly than morphology. For example, Jung et al. (2018) used the Yonsei Zoom-in Cluster Simulation (YZiCS), a zoom-in simulation of 16 clusters with $13.6 < \log(M_{200}/\mathrm{M}_{\odot}) < 15$, and found that 34% of galaxies with $\log(\mathrm{M}_{\star}/\mathrm{M}_{\odot}) > 9$ are gas-poor before infall, with the fraction increasing in higher-mass clusters.

Observationally, O24 compared QF and EF of field galaxies with those in zone 7 of the PPS to assess the degree of pre-processing on star formation and morphology. They found that pre-processing affects both properties, but the impact on star formation is stronger. In groups, pre-processed fractions range from $\sim$ 10–30 % for QF and $\sim$ 0–20 % for EF, with high-mass group galaxies showing negligible pre-processed morphology. Both QF- and EF-based pre-processed fractions decrease with stellar mass, and the values for clusters are comparable to or slightly higher than those for groups. Similarly, Lopes et al. (2024) found that beyond $2R_{200}$, late-type fractions in groups and clusters remain about 10 % higher than star-forming fractions, suggesting that morphological transformation lags behind quenching.

4.4 Quenching Mechanisms

Here, we discuss some potential mechanisms responsible for quenching galaxies with $\log(M_\star/M_\odot) \geq 10$. We first focus on central galaxies as they are free from environmental effects such as ram pressure and starvation/strangulation.

4.4.1 AGN Feedback as the Primary Quenching Mechanism in Centrals

In TNG, the dominant quenching mechanism depends largely on galaxy mass. Donnari et al. (2021a) show that only galaxies with $\log(M_\star/M_\odot) > 10$ are able to quench before infall. This transition can also be seen in Figure A.6, where almost all low-mass centrals remain star-forming. Zinger et al. (2020) show that this transition corresponds to the shift from the thermal (high-accretion) AGN feedback mode to the kinetic (low-accretion) mode, which typically occurs at $\log(M_\star/M_\odot) \sim 10$, or more precisely once the SMBH exceeds $M_{\rm BH} \sim 10^{7.6}$ $M_\odot$.

Kinetic feedback not only ejects gas from the ISM into the CGM, but also raises the entropy of the CGM, which lengthens its cooling time (Zinger et al., 2020). While SMBHs in the thermal mode inject large amounts of energy, this energy couples inefficiently to the ISM due to numerical effects and the adopted subgrid cooling prescriptions for dense star-forming gas in TNG (Terrazas et al., 2020). Terrazas et al. (2020) also find that once $\log(M_\star/M_\odot) > 10.5$, the energy from kinetic feedback can exceed the binding energy of the gas, removing a large amount of gas. This explains why our high-mass centrals steadily lose gas over time (bottom row of Figure 3.5). We have further confirmed that the centrals within the intermediate-mass bin that

lose gas in Figure 3.5 are in fact galaxies that have grown past $\log(M_\star/M_\odot) \sim 10.5$ by $z = 0$. Moreover, Zinger et al. (2020) show that kinetic feedback can significantly raise the CGM entropy of galaxies with $\log(M_\star/M_\odot) > 10.5$, increasing the cooling time to > 10 Gyr. This suppresses the replenishment of cold gas and quenches star formation in a way that resembles starvation. Nevertheless, the reduction in gas binding energy caused by limited resolution may make ejection overly efficient, leading to high-mass galaxies in TNG being overquenched compared to observations in the local universe (Heß & Springel, 2012; Steinhauser et al., 2016; Rodríguez-Cardoso et al., 2025). Finally, while centrals are typically unaffected by environmental mechanisms, it is worth noting that processes acting on satellites can indirectly influence them. Rohr et al. (2023) show that ram-pressure stripping of satellites within a shared halo can provide a significant amount of cold gas into the halo, which may subsequently accrete onto centrals.

4.4.2 Enhanced AGN Feedback in Satellite Quenching

From Figure 3.5, satellites in groups and clusters lose gas more rapidly than centrals after infall, indicating additional environmental processes beyond AGN feedback. For satellites with $\log(M_\star/M_\odot) > 10$, dense environments suppress gas accretion onto their SMBHs, often maintaining or triggering a transition to kinetic feedback mode (Kurinchi-Vendhan et al., 2025).

Satellites with $\log(M_\star/M_\odot) > 10.5$ are less susceptible to direct ram-pressure stripping due to their deeper gravitational potential wells (e.g. Goubert et al., 2024). However, their SMBHs are typically massive enough to sustain low-accretion kinetic feedback, which efficiently prevents gas cooling and can eject gas from the ISM and CGM

(Terrazas et al., 2020; Zinger et al., 2020; Rohr et al., 2023). Starvation (or strangulation) then further limits fresh gas supply, driving rapid quenching. In groups, recently infallen high-mass satellites (< 3 Gyr) often resemble centrals in gas content and star formation, consistent with weaker RPS compared to clusters. As noted in Section 3.3, the increase in gas mass for satellites with infall times around 4 Gyr may be linked to on-going mergers that trigger star formation or even starbursts that rapidly consume the available gas (Faria et al., 2025).

For intermediate-mass satellites ($10 \leq \log(\mathrm{M}_\star/\mathrm{M}_\odot) < 10.4$), the picture is more complex. Rohr et al. (2023) showed that peak RPS phases occur within ∼1–2 Gyr of infall in $\mathrm{M}_{halo}/\mathrm{M}_\odot \sim 10^{12.5}$–$10^{13.5}$ halos, and up to ~ 5 Gyr in more massive halos, with stripping effective not only in the core but out to $\sim 2R_{200}$. This result is consistent with our Figures 3.5 and A.7, which show that cluster satellites can lose $\sim$ 50% of their gas near 1 R_{200}. If the SMBH is sufficiently massive, reduced gas accretion can drive a transition to kinetic mode, compounding gas removal. Conversely, if enough gas remains available and is funneled inward by RPS or interactions, the SMBH may instead remain in thermal mode, with gas loss dominated by stripping (Kurinchi-Vendhan et al., 2025).

Overall, these results support a picture in which environment both removes gas directly and suppresses further gas accretion, while the SMBH mass sets how efficiently any remaining gas is expelled or prevented from cooling. In fact, Goubert et al. (2024) find that quenching in massive galaxies correlates most strongly with M_{BH} rather than halo mass or local density across multiple simulations (EAGLE and TNG) as well as in observations.

4.5 Mechanisms of Morphological Evolution

For high-mass centrals ($\log(M_\star/M_\odot) > 10.5$), counter-rotating stellar particles are primarily built up through mergers. In Illustris, Rodriguez-Gomez et al. (2017) find that gas-poor mergers tend to transform centrals with $\log(M_\star/M_\odot) > 11$ into dispersion-dominated systems, whereas gas-rich mergers can sustain massive discs. Similar results are found in EAGLE, where Santucci et al. (2024) show that the fraction of counter-rotating stars in centrals correlates with the number of dry mergers but shows no dependence on the number of wet mergers. In TNG100, Rodríguez et al. (2025) find that ellipticals ($B/T_{\epsilon<0}$ between 0.87 and 1) tend to acquire a larger fraction of their stellar mass through mergers compared to disc systems ($B/T_{\epsilon<0} < 0.32$). Ellipticals experience more regular mergers, while mergers in discs are typically absent in the past 5 Gyr. Case studies in TNG50 indicate that major mergers cause uniform dynamical heating of pre-existing stars within one effective radius, after which new stars form a cold disc (Zhang et al., 2025).

However, the correlation between mergers and kinematic morphology appears to weaken in lower-mass centrals (Rodriguez-Gomez et al., 2017; Joshi et al., 2020; Rodríguez et al., 2025). Rodriguez-Gomez et al. (2017) show that these galaxies experience fewer mergers overall, but a higher fraction of these are wet mergers. This combination of fewer mergers and abundant gas allows ongoing star formation to replenish dynamically cold orbits, weakening the link between mergers and final kinematic morphology. While dynamically cold stars can be heated over time (Zhang et al., 2025), some studies argue that a high accretion angle of the gas relative to the rotation axis of the disc (Santucci et al., 2024; Peirani et al., 2025), can also contribute to the formation of counter-rotating orbits. These results suggest that while

various reasons could lead to a higher fraction of counter-rotating stars, the extent of morphological transformation is primarily regulated by ongoing star formation. This helps explain why intermediate-mass centrals in our sample become more disky over time, whereas high-mass centrals become increasingly bulge-dominated, consistent with the onset of efficient kinetic feedback at the high-mass end (see Section 4.4).

Similarly, this also explains the divergent evolutionary paths of intermediate-mass satellites and centrals, as satellites tend to quench soon after infall. However, this cannot explain why high-mass centrals and satellites exhibit the same degree of morphological transformation over time, especially given that mergers are expected to be rare in clusters. Joshi et al. (2020) find that the final morphology of cluster disc satellites in TNG is strongly correlated with the number of pericentric passages, rather than infall time, with similar results reported by van den Bosch et al. (2016). Łokas (2020) also finds that the greater the total integrated force experienced by cluster satellites after infall, the more likely they are to develop non-disky morphologies.

These results highlight the complex interplay between galaxy–galaxy interactions, gas accretion, and environment in shaping galaxy morphology and star formation rates, while also underscoring the limitations of the simulations. In the next chapter, we summarize our findings and discuss directions for future work.

Chapter 5

Conclusion

In this thesis we study the environmental dependence of galaxy star formation rates and morphologies using the state-of-the-art hydrodynamic simulation IllustrisTNG100. We focus on how these properties evolve as galaxies fall into groups and clusters. We aim to answer two central questions: (1) Can TNG reproduce the environmental trends of star formation and morphology observed in SDSS? and (2) How do these properties change after galaxies become satellites?

To address the first question, we analyze satellite galaxies with stellar masses above $10^{9.5}\mathrm{M}_{\odot}$ and study how their star formation and morphology at $z = 0$ depend on their infall time. We first examine the consistency between the observationally accessible infall time ($T_{\mathrm{inf,PPS}}$) and the true infall time ($T_{\mathrm{inf,true}}$). We then compare the quenched fraction (QF) at $z = 0$ as a function of $T_{\mathrm{inf,PPS}}$ to low-redshift SDSS measurements from Oxland et al. (2024). We also compare the early-type fraction by using four metrics: (a) $B/T_{\epsilon<0} \geq 0.6$, (b) $B/T_{\epsilon<0.7} \geq 0.7$, (c) Sérsic index ≥ 3, and (d) $P_{late} \leq 0.4$. The main conclusions are:

- The trends in QF as a function of $T_{\rm inf,true}$ and $T_{\rm inf,PPS}$ are broadly similar; however, projection effects can introduce artificial features into the $T_{\rm inf,PPS}$–based trends and should therefore be interpreted with caution.

- In TNG, SFRs and morphologies change as a function of infall time in a way similar to low-z observations, but low mass satellites in TNG100 are systematically more quenched than observed galaxies.

- The four morphology indicators yield inconsistent classifications, highlighting the difficulty of bridging morphological definitions in simulations and observations.

To answer the second question we restrict our sample to galaxies with $\mathrm{M}_\star \geq 10^{10}\mathrm{M}_\odot$ at the time of infall, ensuring kinematic morphology measures are robust against numerical heating (Wilkinson et al., 2023; Ludlow et al., 2023; Zeng et al., 2024). We compare each satellite's properties (stellar mass, offset from the star-forming main sequence, total gas mass, and $B/T_{\epsilon<0}$) between infall and $z = 0$, using a mass-matched sample of centrals as a control to isolate environmental effects. Our principal findings are:

- Centrals grow steadily in stellar mass over time, while satellites show little growth in groups and no growth in clusters after infall.

- Satellites evolve rapidly off the main sequence after infall, whereas intermediate mass centrals sustain star formation, and high-mass centrals quench gradually over time.

- After infall, satellites become slightly more bulge-dominated. In contrast, intermediate mass centrals tend to become more disk-dominated, while high-mass

centrals show an increase in $B/T_{\epsilon<0}$ comparable to that of satellites.

- Pre-processing has minimal impact on morphology and stellar mass but can strongly suppress star formation and remove gas, which is consistent with observations.

In conclusion, we find that galaxies in TNG broadly reproduce the observed environmental trends in SDSS: satellites show an increasing quenched fraction with infall time, while morphology exhibits no strong dependence on infall time. A closer examination of satellite star formation activity, gas mass, and morphology reveals that quenching in dense environments is rapid and efficient, whereas morphological transformation is more gradual and proceeds on longer timescales. Our results support a picture in which quenching of galaxies with $\log(M_\star/M_\odot) > 10$ in TNG is primarily driven by AGN feedback (e.g. Donnari et al., 2021a; Terrazas et al., 2020; Zinger et al., 2020), with environmental gas stripping in satellites further accelerating the process (Kurinchi-Vendhan et al., 2025). The shutdown of star formation also suppresses the replenishment of new stars on dynamically cold orbits, leading to a gradual increase in $B/T_{\epsilon<0}$ after infall (Joshi et al., 2020). While these findings clarify how star formation and morphology evolve in different environments, they also highlight several open questions and limitations that point to the need for future work.

Future Work

While our analysis provides new insights into the environmental dependence of galaxy evolution, several limitations remain. The detailed physical mechanisms driving morphological transformation, especially in low-mass satellites ($\log(M_\star/M_\odot) < 10$), are

not yet fully understood. These galaxies are expected to be more susceptible to environmental effects, but limited numerical resolution in the simulation reduces the robustness of their kinematic measurements. This could be addressed by targeting higher-resolution simulations. Furthermore, the limited volume of TNG100 restricts our sample to a relatively small number of massive clusters and high-mass galaxies, reducing the statistical power to study high-density environments. Extending our analysis to larger-volume simulations with comparable resolution would improve the sampling of massive clusters and high-mass satellites, allowing for more robust statistical conclusions. Finally, analyzing higher-redshift observations and comparing them with mock TNG images would allow a more direct and consistent comparison of galaxy morphologies across cosmic time.

Appendix A

Supplementary Plots

The following supplementary plots provide additional support for the results presented in the main text. They include the star-forming main sequence across 11 redshifts, tests of methodology, variations in galaxy classification thresholds, evolution of low-mass galaxy properties, and other galaxy property trends. These figures demonstrate the robustness of the trends discussed in the main text and provide further context for readers interested in the detailed analysis.

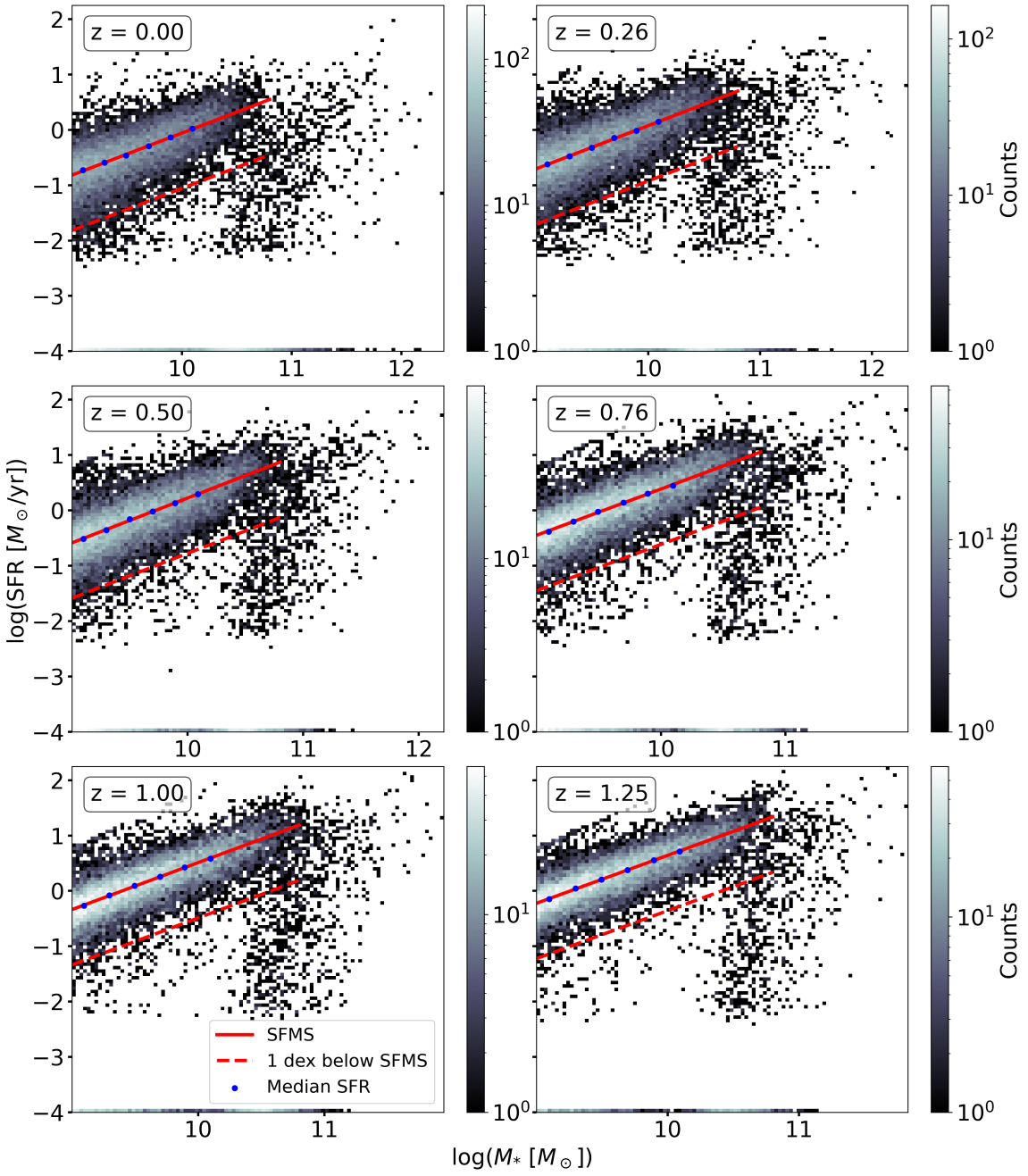

Figure A.1: Star forming main sequence of TNG100 using SFR_{200} across 11 redshifts. Panel layout and line styles follow those in Figure 2.5.

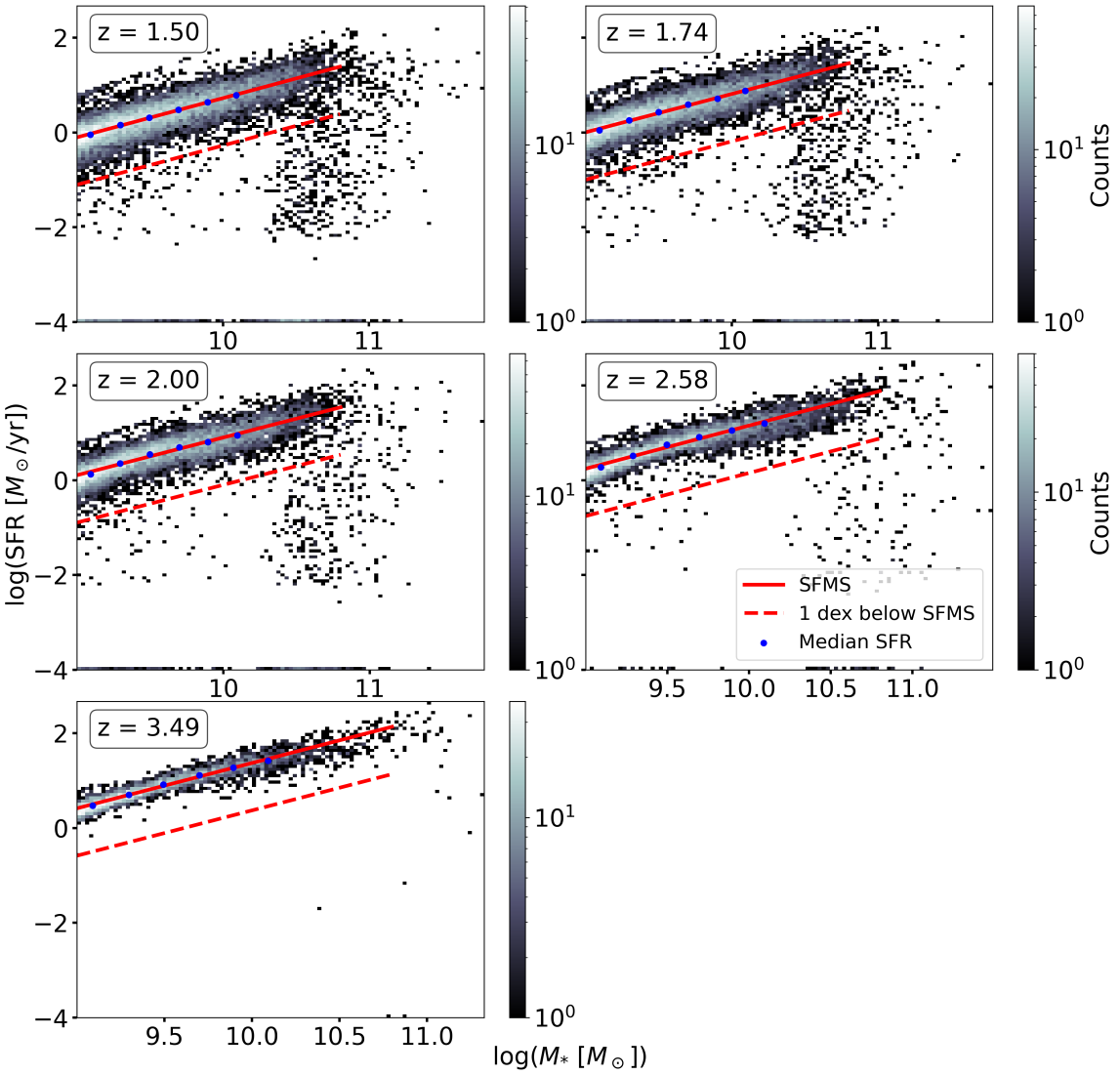

Figure A.2: Same as Figure A.1 but for earlier snapshots/redshifts.

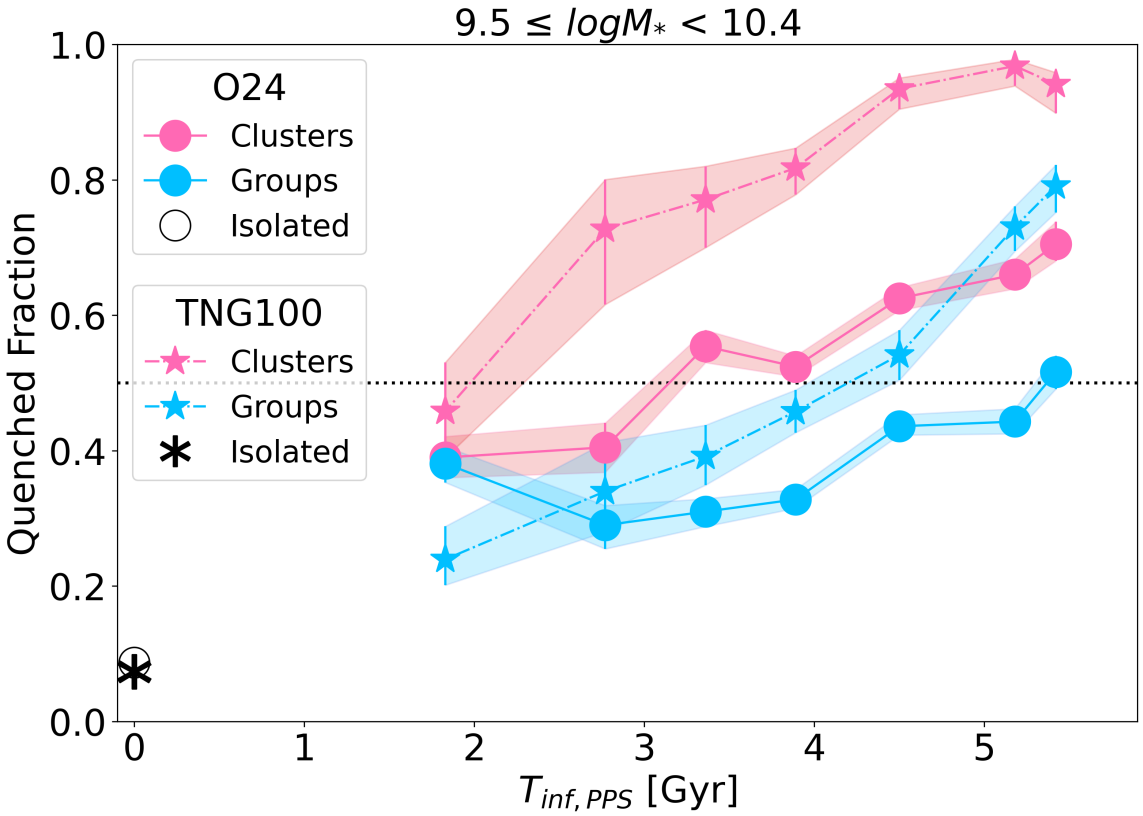

Figure A.3: Same as Figure 3.2 but includes interloper population. In general, adding interlopers slightly decreases the quenched fraction (by less than a few percent) in zones corresponding to short infall times. However, the overall trends remain nearly unchanged from Figure 3.2, and TNG still overpredicts the quenched fraction in dense environments.

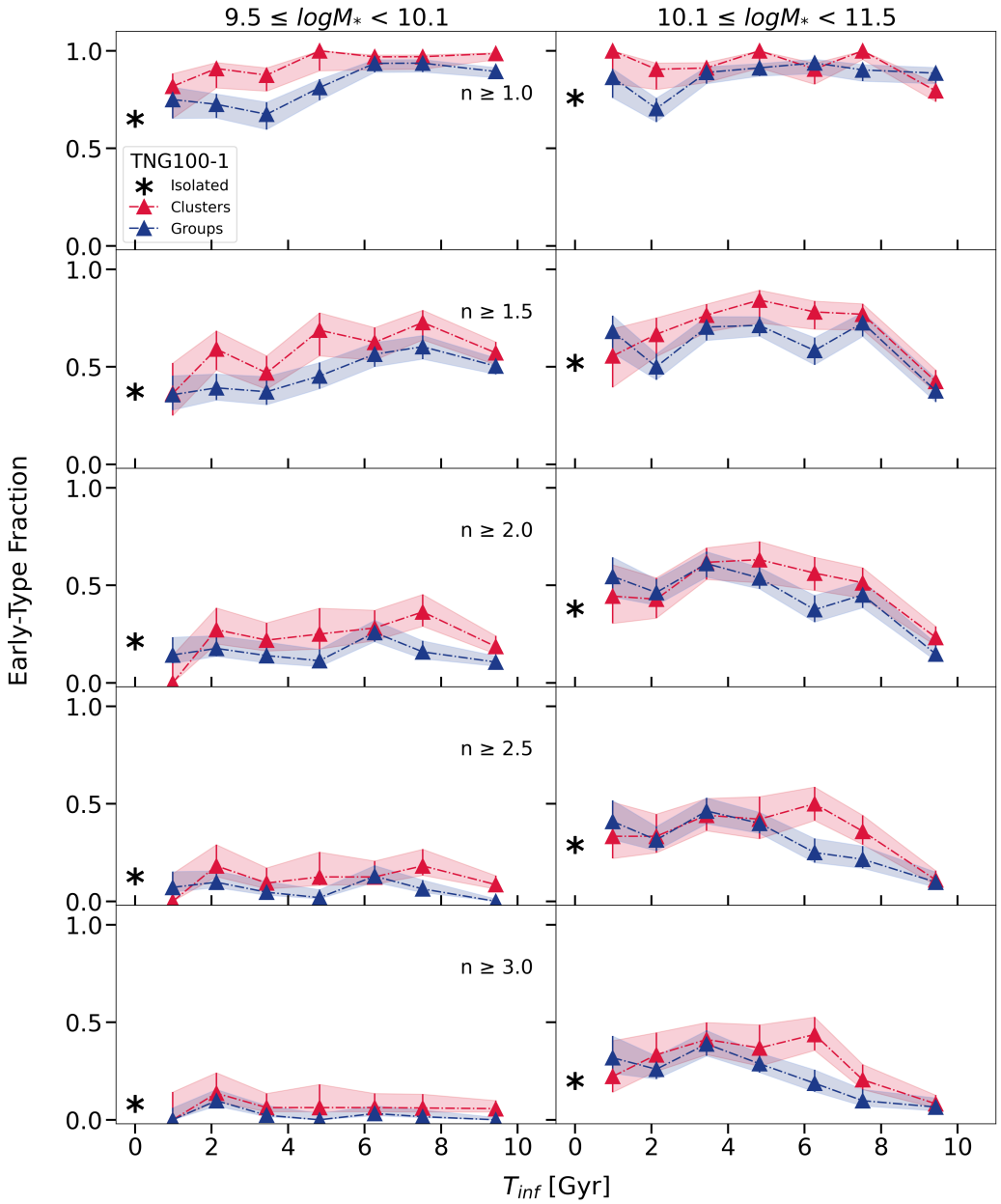

Figure A.4: Early-type fraction (EF), defined using the i-band Sérsic index, as a function of infall time. Different rows correspond to different Sérsic -index thresholds used to classify early-type galaxies. The threshold adopted in Section 3.2 corresponds to the bottom row. While varying the Sérsic -index threshold affects the EF values, it does not significantly alter the overall trend. The results show no substantial dependence on either the environments or infall time.

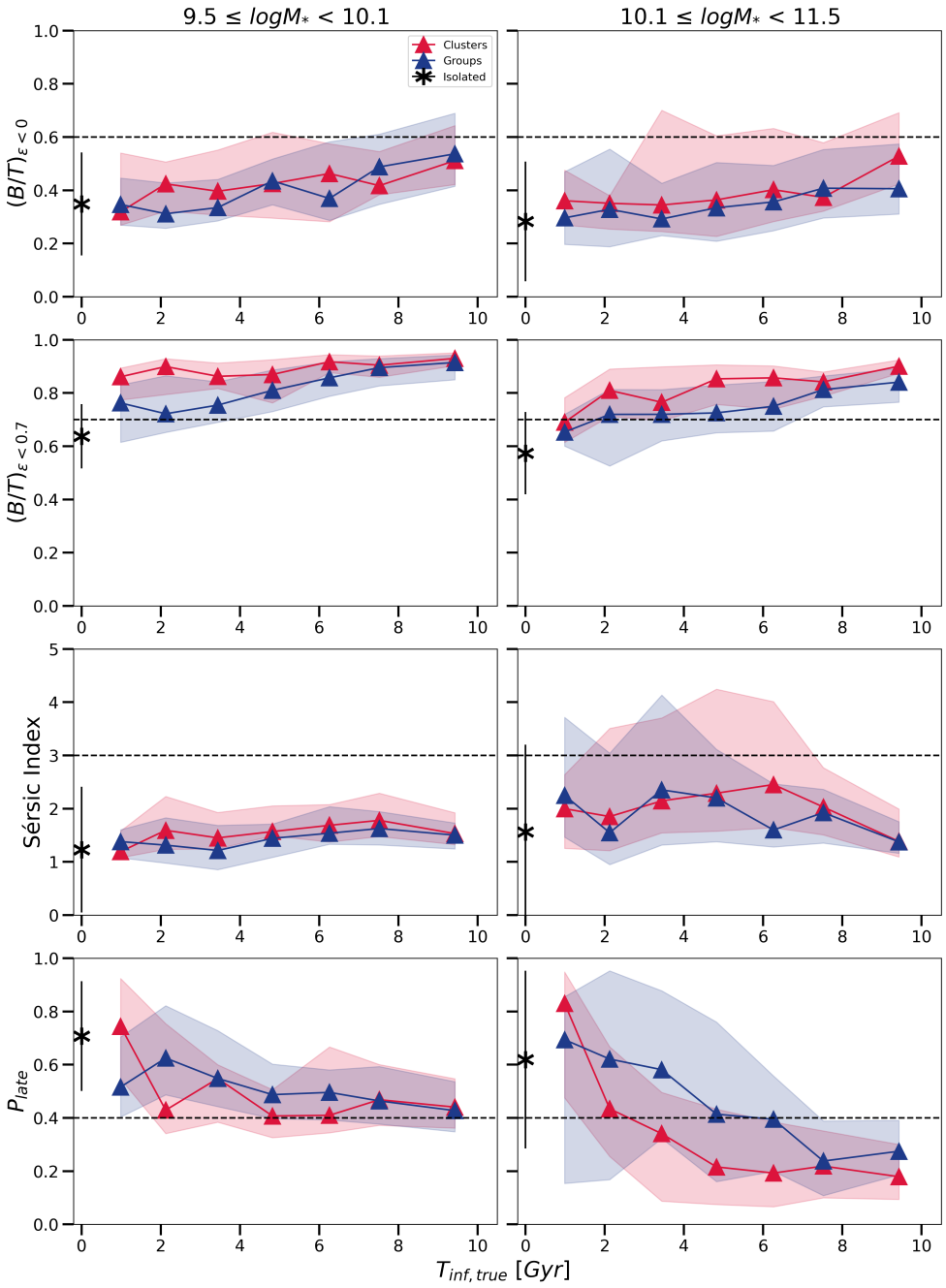

Figure A.5: The median values of $B/T_{\epsilon<0}$, $B/T_{\epsilon<0.7}$, Sérsic index, and P_{late} as a function of $T_{\rm inf,true}$. The two columns and colour schemes follow those in Figure 3.1. Shaded regions indicate the 25th and 75th percentiles within each time bin. Black dashed lines mark the thresholds used to distinguish early-type galaxies. The median value of each morphology indicator shows a weak dependence on infall time.

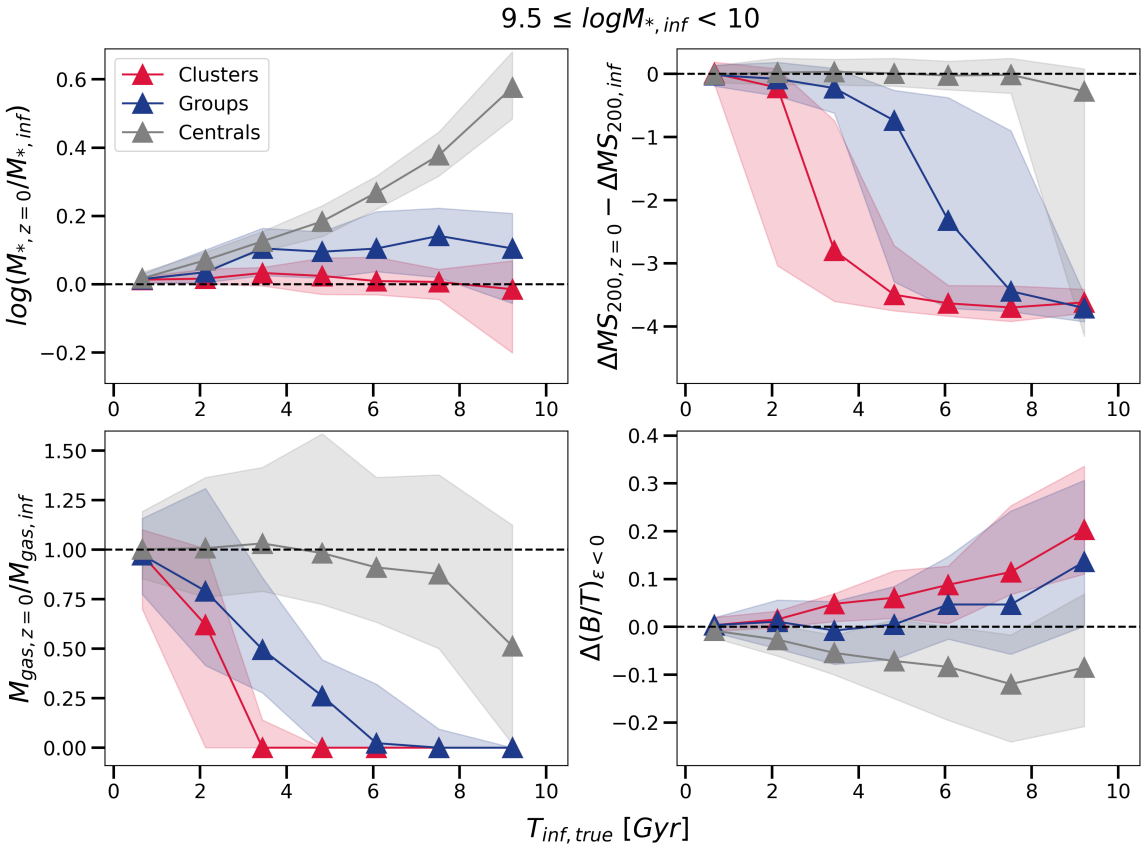

Figure A.6: Change in galaxy stellar mass, main sequence offset, gas mass, and $B/T_{\epsilon<0}$ from infall to z = 0, as a function of true infall time for low-mass galaxies. Panel layout, line styles, and the shaded regions follow those in Figure 3.5. Low-mass galaxies evolve similarly to those with $10 \leq \log(M_\star/M_\odot) < 10.4$. Satellites quench and develop more prominent bulges after infall, but with faster and stronger bulge growth. Centrals maintain steadier star formation and show a larger increase in diskiness compared to intermediate-mass centrals. The large fraction of quenched centrals with long evolutionary timescales (> 8 Gyr) are likely galaxies that grew to $\log(M_\star/M_\odot) > 10.5$ by $z = 0$.

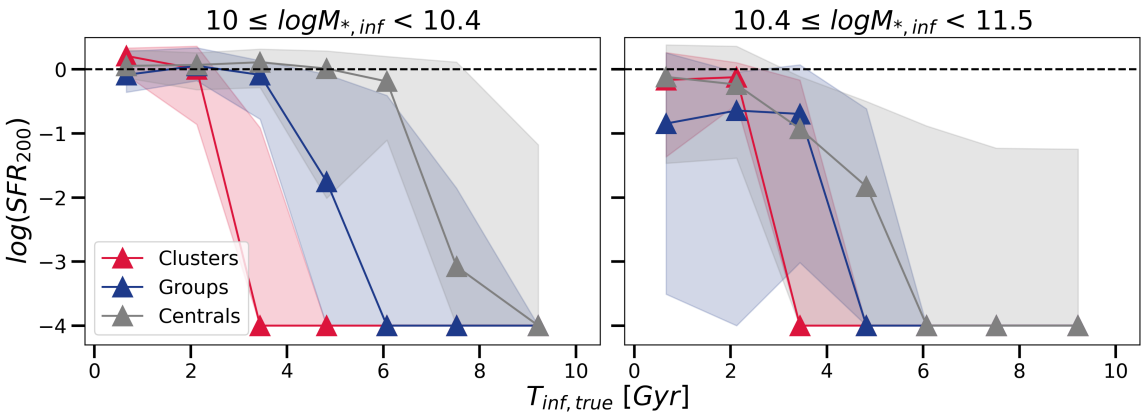

Figure A.7: $\log(\mathrm{SFR}_{200}\ [\mathrm{M}_\odot\ \mathrm{yr}^{-1}])$ at $z = 0$ as a function of $T_{\mathrm{inf,true}}$. Panel layout, line styles, and shaded regions are the same as in Figure 3.5.

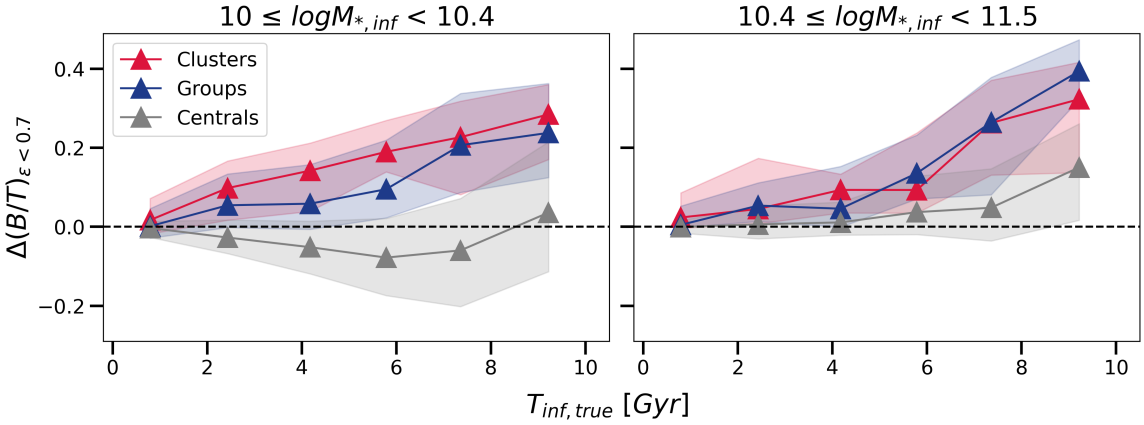

Figure A.8: Difference in $B/T_{\epsilon<0.7}$ between $z = 0$ and infall as a function of $T_{\mathrm{inf,true}}$. Panel layout, line styles, and shaded regions are the same as in Figure 3.5. Values above the dashed line indicate an increase in $B/T_{\epsilon<0.7}$. Similar to the change in $B/T_{\epsilon<0}$ shown in Figure 3.6, satellites and high-mass centrals generally become more bulge-dominated over time, while intermediate-mass centrals tend to build up their disks. However, the evolution of $B/T_{\epsilon<0.7}$ shows a stronger dependence on environment.

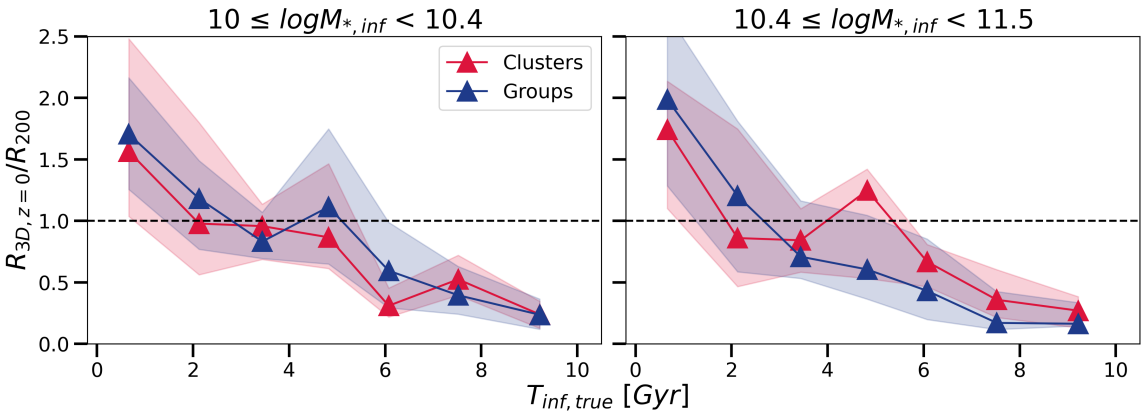

Figure A.9: 3D halo-centric distance of satellites at $z = 0$ as a function of $T_{\rm inf,true}$. Panel layout, line styles, and shaded regions are the same as in Figure 3.5. The dashed line denotes one virial radius. Satellites follow a zig-zag trajectory as they infall, which can be used to infer the occurrence of pericentric passage. Cluster satellites with infall times between 2 to 4 Gyr are likely still undergoing the first preicentric passage. For group satellites, the first pericentric passage appears to occur ~ 3 Gyr after infall.

Appendix B

Colour Diagram

As mentioned in Section 1.1.3, galaxy colours can also serve as indicators of star formation activity. We use the U, V, and J magnitudes measured from mock images by Gebek et al. (2024), which include the effects of dust on starlight. This catalog is available at two redshifts: $z = 0$ and $z = 0.1$. To mimic observations without dust correction, we use a random orientation. Magnitudes are measured within twice the stellar half-mass radius.

Define Quenched Galaxies

Figure B.1 shows the UVJ diagram of TNG100 galaxies at $z = 0$, based on measurements from Gebek et al. (2024). Galaxies are clearly separated into two populations: quenched/red galaxies near the top right, and star-forming/blue galaxies near the middle. To separate the two populations, we start with the initial threshold from Donnari et al. (2019), based on their earlier UVJ catalog (red dashed line in the left panel). We then adjust the slope and intercept until the galaxy distribution appears bimodal (right panel). Finally, we define quenched/red galaxies as those located

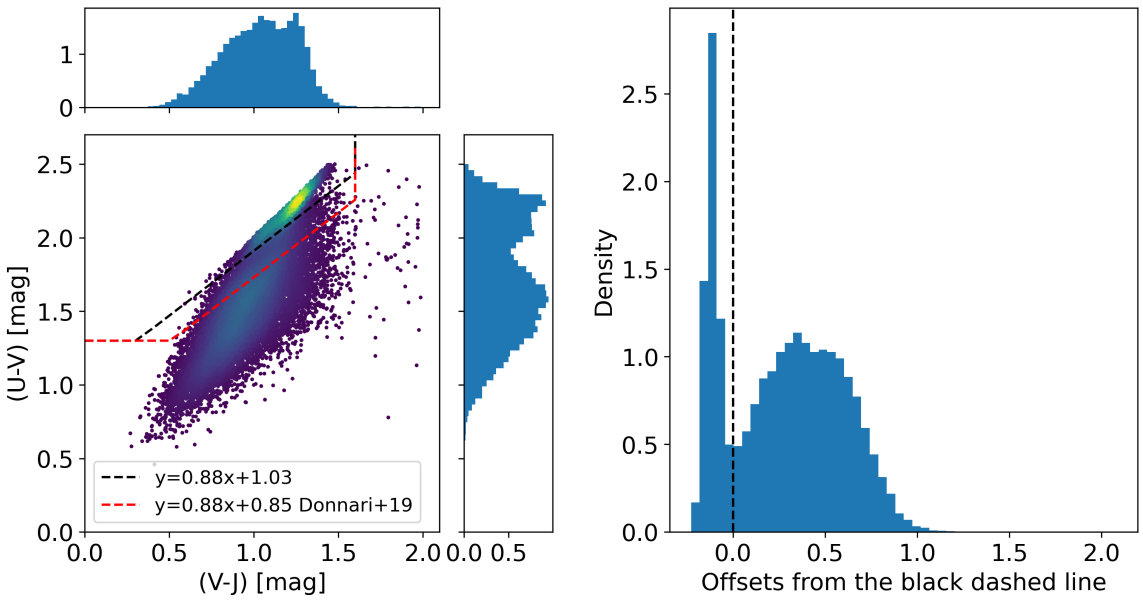

Figure B.1: Use of the UVJ colour diagram to identify quenched galaxies at z = 0. Left panel: The UVJ diagram at z = 0, colour-coded by galaxy number density. Quenched and star-forming galaxies lie above and below the black dashed line, respectively. The red dashed line shows the previous separation threshold from Donnari et al. (2019), based on UVJ magnitudes modeled using the method of Nelson et al. (2018). Right panel: The distribution of galaxy offsets from the black dashed line in the left panel. The updated threshold is adjusted to produce a bimodal distribution.

above the black line.

Quenched Fraction vs Infall Time

Figure B.2 shows the QF as a function of $T_{\mathrm{inf,PPS}}$ and $T_{\mathrm{inf,true}}$. The results closely match those in Section 3.1, where QF increases with infall time and the trend is steeper in clusters than in groups. The only notable difference appears in the higher mass bin, where group satellites show a nearly constant QF during the first 4 Gyr after infall.

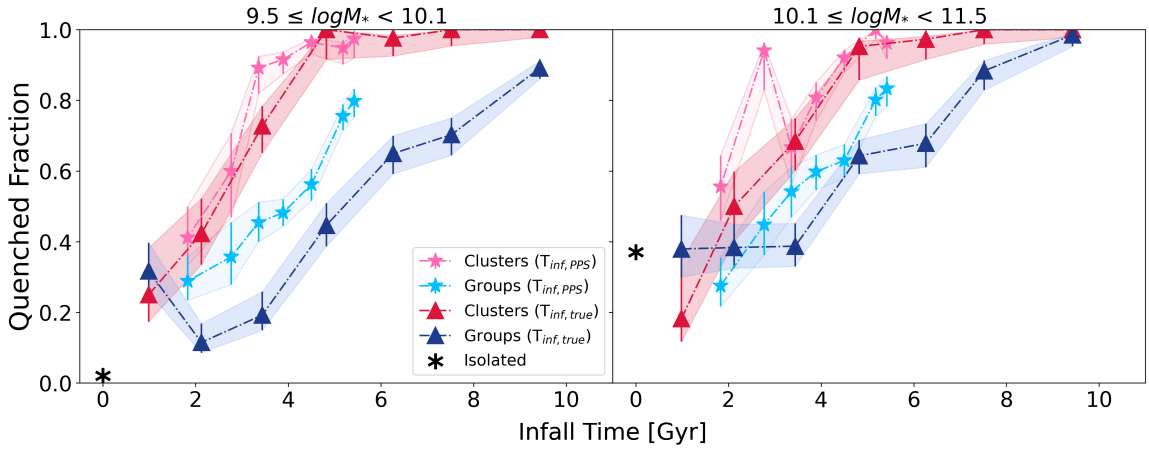

Figure B.2: Same as Figure 3.1, but using U, V, and J magnitudes to identify quenched galaxies.

Bibliography

Abadi M. G., Navarro J. F., Steinmetz M., Eke V. R., 2003, ApJ, 597, 21

Arthur J., et al., 2019, MNRAS, 484, 3968

Bahé Y. M., et al., 2017, MNRAS, 470, 4186

Barai P., Viel M., Murante G., Gaspari M., Borgani S., 2014, MNRAS, 437, 1456

Bédorf J., Portegies Zwart S., 2013, MNRAS, 431, 767

Boissier S., 2013, in Oswalt T. D., Keel W. C., eds, , Vol. 6, Planets, Stars and Stellar Systems. Volume 6: Extragalactic Astronomy and Cosmology. Springer, Dordrecht, p. 141, doi:10.1007/978-94-007-5609-0˙3

Boselli A., Cortese L., Boquien M., Boissier S., Catinella B., Gavazzi G., Lagos C., Saintonge A., 2014, A&A, 564, A67

Bottrell C., Torrey P., Simard L., Ellison S. L., 2017, MNRAS, 467, 2879

Brinchmann J., Charlot S., White S. D. M., Tremonti C., Kauffmann G., Heckman T., Brinkmann J., 2004, MNRAS, 351, 1151

Bundy K., et al., 2010, ApJ, 719, 1969

Cameron E., 2011, Publ. Astron. Soc. Aust., 28, 128

Carroll B. W., Ostlie D. A., 2017, An introduction to modern astrophysics, Second Edition. Cambridge University Press, Cambridge, United Kingdom

Celiz B. M., Navarro J. F., Abadi M. G., Springel V., 2025, A&A, 699, A12

Chabrier G., 2003, PASP, 115, 763

Correa C. A., Schaye J., Clauwens B., Bower R. G., Crain R. A., Schaller M., Theuns T., Thob A. C. R., 2017, MNRAS, 472, L45

Cortese L., Catinella B., Smith R., 2021, Publ. Astron. Soc. Aust., 38, e035

Daddi E., et al., 2007, ApJ, 670, 156

Ding Y., Zhu L., Pillepich A., van de Ven G., Corsini E. M., Iodice E., Pinna F., 2024, A&A, 686, A184

Dolag K., Borgani S., Murante G., Springel V., 2009, MNRAS, 399, 497

Donnari M., et al., 2019, MNRAS, 485, 4817

Donnari M., et al., 2021a, MNRAS, 500, 4004

Donnari M., Pillepich A., Nelson D., Marinacci F., Vogelsberger M., Hernquist L., 2021b, MNRAS, 506, 4760

Dressler A., 1980, ApJ, 236, 351

Dubois Y., Gavazzi R., Peirani S., Silk J., 2013, MNRAS, 433, 3297

Dubois Y., et al., 2014, MNRAS, 444, 1453

Dubois Y., Peirani S., Pichon C., Devriendt J., Gavazzi R., Welker C., Volonteri M., 2016, MNRAS, 463, 3948

Džudžar R., et al., 2019, MNRAS, 483, 5409

Fang J. J., et al., 2018, ApJ, 858, 100

Faria L., Patton D. R., Courteau S., Ellison S., Brown W., 2025, MNRAS, 537, 915

Gebek A., Trčka A., Baes M., Martorano M., Pillepich A., Kapoor A. U., Nersesian A., van der Wel A., 2024, MNRAS, 531, 3839

Gebek A., et al., 2025, A&A, 695, A90

Genel S., Fall S. M., Hernquist L., Vogelsberger M., Snyder G. F., Rodriguez-Gomez V., Sijacki D., Springel V., 2015, ApJL, 804, L40

Genel S., et al., 2018, MNRAS, 474, 3976

Gensior J., Kruijssen J. M. D., Keller B. W., 2020, MNRAS, 495, 199

George A., et al., 2024, MNRAS, 528, 4797

Gillman S., et al., 2019, MNRAS, 486, 175

Goto T., Yamauchi C., Fujita Y., Okamura S., Sekiguchi M., Smail I., Bernardi M., Gomez P. L., 2003, MNRAS, 346, 601

Goubert P. H., Bluck A. F. L., Piotrowska J. M., Maiolino R., 2024, MNRAS, 528, 4891

Governato F., et al., 2010, Nature, 463, 203

Gunn J. E., Gott III J. R., 1972, ApJ, 176, 1

Haines C. P., et al., 2015, ApJ, 806, 101

Heß S., Springel V., 2012, MNRAS, 426, 3112

Hubble E. P., 1926, ApJ, 64, 321

Hubble E. P., 1929, ApJ, 69, 103

Hubble E., Humason M. L., 1931, ApJ, 74, 43

Huertas-Company M., et al., 2019, MNRAS, 489, 1859

Inoue A. K., 2011, Earth, Planets and Space, 63, 1027

Jang J. K., et al., 2023, ApJ, 950, 4

Joshi G. D., Pillepich A., Nelson D., Marinacci F., Springel V., Rodriguez-Gomez V., Vogelsberger M., Hernquist L., 2020, MNRAS, 496, 2673

Jung S. L., Choi H., Wong O. I., Kimm T., Chung A., Yi S. K., 2018, ApJ, 865, 156

Kauffmann G., White S. D. M., Heckman T. M., Ménard B., Brinchmann J., Charlot S., Tremonti C., Brinkmann J., 2004, MNRAS, 353, 713

Kaviraj S., 2025, arXiv e-prints, p. arXiv:2506.09136

Kelkar K., Gray M. E., Aragón-Salamanca A., Rudnick G., Milvang-Jensen B., Jablonka P., Schrabback T., 2017, MNRAS, 469, 4551

Kennicutt Jr. R. C., 1992, ApJ, 388, 310

Kennicutt Jr. R. C., 1998, ApJ, 498, 541

Kennicutt R. C., Evans N. J., 2012, ARAA, 50, 531

Kolcu T., Crossett J. P., Bellhouse C., McGee S., 2022, MNRAS, 515, 5877

Koprowski M. P., Wijesekera J. V., Dunlop J. S., McLeod D. J., Michałowski M. J., Lisiecki K., McLure R. J., 2024, A&A, 691, A164

Kukstas E., McCarthy I. G., Baldry I. K., Font A. S., 2020, MNRAS, 496, 2241

Kukstas E., et al., 2023, MNRAS, 518, 4782

Kurinchi-Vendhan S., Rohr E., Pillepich A., Zinger E., Ayromlou M., Joshi G. D., 2025, arXiv e-prints, p. arXiv:2506.05474

Lacerna I., Rodríguez-Puebla A., Avila-Reese V., Hernández-Toledo H. M., 2014, ApJ, 788, 29

Lagos C. d. P., Theuns T., Stevens A. R. H., Cortese L., Padilla N. D., Davis T. A., Contreras S., Croton D., 2017, MNRAS, 464, 3850

Lazar I., Kaviraj S., Watkins A. E., Martin G., Bichang'a B., Jackson R. A., 2024, MNRAS, 529, 499

Levis S., Coenda V., Muriel H., de los Rios M., Ragone-Figueroa C., Martínez H. J., Ruiz A. N., 2025, A&A, 698, A57

Lin C.-H., Chen K.-J., Hwang C.-Y., 2023, ApJ, 952, 121

Lintott C. J., et al., 2008, MNRAS, 389, 1179

Lintott C., et al., 2011, MNRAS, 410, 166

Łokas E. L., 2020, A&A, 638, A133

Lopes P. A. A., Ribeiro A. L. B., Brambila D., 2024, MNRAS, 527, L19

Lotz M., Remus R.-S., Dolag K., Biviano A., Burkert A., 2019, MNRAS, 488, 5370

Ludlow A. D., Fall S. M., Schaye J., Obreschkow D., 2021, MNRAS, 508, 5114

Ludlow A. D., Fall S. M., Wilkinson M. J., Schaye J., Obreschkow D., 2023, MNRAS, 525, 5614

Maier C., et al., 2016, A&A, 590, A108

Mamon G. A., 2007, in Saviane I., Ivanov V. D., Borissova J., eds, Groups of Galaxies in the Nearby Universe. p. 203 (arXiv:astro-ph/0607482), doi:10.1007/978-3-540-71173-5˙35

Marinacci F., Pakmor R., Springel V., 2014, MNRAS, 437, 1750

Marinacci F., et al., 2018, MNRAS, 480, 5113

Martig M., Bournaud F., Teyssier R., Dekel A., 2009, ApJ, 707, 250

Martin G., Kaviraj S., Hocking A., Read S. C., Geach J. E., 2020, MNRAS, 491, 1408

Martínez H. J., Coenda V., Muriel H., de los Rios M., Ruiz A. N., 2023, MNRAS, 519, 4360

McAlpine S., Harrison C. M., Rosario D. J., Alexander D. M., Ellison S. L., Johansson P. H., Patton D. R., 2020, MNRAS, 494, 5713

McDonough B., Curtis O., Brainerd T. G., 2023, ApJ, 958, 19

Mei S., et al., 2023, A&A, 670, A58

Naiman J. P., et al., 2018, MNRAS, 477, 1206

Nelson D., et al., 2018, MNRAS, 475, 624

Obreja A., Stinson G. S., Dutton A. A., Macciò A. V., Wang L., Kang X., 2016, MNRAS, 459, 467

Oxland M., Parker L. C., de Carvalho R. R., Sampaio V. M., 2024, MNRAS, 529, 3651

Pannella M., et al., 2015, ApJ, 807, 141

Park S.-M., Chun K., Shin J., Jeong H., Lee J. H., Pak M., Smith R., Kim J.-W., 2023, ApJ, 954, 98

Pasquali A., Smith R., Gallazzi A., De Lucia G., Zibetti S., Hirschmann M., Yi S. K., 2019, MNRAS, 484, 1702

Pearson W. J., Wang L., Brough S., Holwerda B. W., Hopkins A. M., Loveday J., 2021, A&A, 646, A151

Peirani S., Suto Y., Han S., Yi S. K., Dubois Y., Kraljic K., Park M., Pichon C., 2025, A&A, 696, A45

Pillepich A., et al., 2018a, MNRAS, 473, 4077

Pillepich A., et al., 2018b, MNRAS, 475, 648

Pillepich A., et al., 2019, MNRAS, 490, 3196

Planck Collaboration et al., 2016, A&A, 594, A13

Planck Collaboration et al., 2020, A&A, 641, A6

Rakhi R., et al., 2023, MNRAS, 522, 1196

Rautio R. P. V., Watkins A. E., Comerón S., Salo H., Díaz-García S., Janz J., 2022, A&A, 659, A153

Rhee J., Smith R., Choi H., Contini E., Jung S. L., Han S., Yi S. K., 2020, ApJS, 247, 45

Ricarte A., Tremmel M., Natarajan P., Quinn T., 2020, ApJL, 895, L8

Rinaldi P., et al., 2025, ApJ, 981, 161

Rizzo F., Fraternali F., Iorio G., 2018, MNRAS, 476, 2137

Rodríguez-Cardoso R., et al., 2025, A&A, 698, A303

Rodriguez-Gomez V., et al., 2017, MNRAS, 467, 3083

Rodriguez-Gomez V., et al., 2019, MNRAS, 483, 4140

Rodríguez S., Cristiani V. A., Sales L. V., Abadi M. G., 2025, A&A, 695, A218

Rohr E., Pillepich A., Nelson D., Zinger E., Joshi G. D., Ayromlou M., 2023, MNRAS, 524, 3502

Salim S., et al., 2016, ApJS, 227, 2

Santini P., et al., 2014, A&A, 562, A30

Santucci G., et al., 2024, MNRAS, 528, 2326

Scannapieco C., Gadotti D. A., Jonsson P., White S. D. M., 2010, MNRAS, 407, L41

Schawinski K., et al., 2014, MNRAS, 440, 889

Schaye J., et al., 2015, MNRAS, 446, 521

Sérsic J. L., 1963, Boletin de la Asociacion Argentina de Astronomia La Plata Argentina, 6, 41

Sobral D., Best P. N., Smail I., Mobasher B., Stott J., Nisbet D., 2014, MNRAS, 437, 3516

Springel V., Hernquist L., 2003, MNRAS, 339, 289

Springel V., White S. D. M., Tormen G., Kauffmann G., 2001, MNRAS, 328, 726

Springel V., et al., 2018, MNRAS, 475, 676

Stahler S. W., Palla F., 2004, The Formation of Stars. Wiley-VCH Verlag GmbH & Co. KGaA

Steinhauser D., Schindler S., Springel V., 2016, A&A, 591, A51

Su Y., Fang G., Lu S., Lin Z., 2025, A&A, 699, A184

Sulentic J. W., et al., 2006, A&A, 449, 937

Terrazas B. A., et al., 2020, MNRAS, 493, 1888

Thob A. C. R., et al., 2019, MNRAS, 485, 972

Torrey P., Vogelsberger M., Genel S., Sijacki D., Springel V., Hernquist L., 2014, MNRAS, 438, 1985

Tully R. B., 1987, ApJ, 321, 280

Vika M., Vulcani B., Bamford S. P., Häußler B., Rojas A. L., 2015, A&A, 577, A97

Vogelsberger M., Genel S., Sijacki D., Torrey P., Springel V., Hernquist L., 2013, MNRAS, 436, 3031

Wang L., Xu D., Gao L., Guo Q., Qu Y., Pan J., 2019, MNRAS, 485, 2083

Wang B., Cappellari M., Peng Y., Graham M., 2020, MNRAS, 495, 1958

Wechsler R. H., Tinker J. L., 2018, ARAA, 56, 435

Weinberger R., et al., 2018, MNRAS, 479, 4056

Wetzel A. R., Tinker J. L., Conroy C., 2012, MNRAS, 424, 232

Wilkinson M. J., Ludlow A. D., Lagos C. d. P., Fall S. M., Schaye J., Obreschkow D., 2023, MNRAS, 519, 5942

Winkel N., Pasquali A., Kraljic K., Smith R., Gallazzi A., Jackson T. M., 2021, MNRAS, 505, 4920

Wuyts S., et al., 2007, ApJ, 655, 51

Yang X., Mo H. J., van den Bosch F. C., Pasquali A., Li C., Barden M., 2007, ApJ, 671, 153

Yasuda N., et al., 2001, AJ, 122, 1104

Zasov A. V., Khoperskov A. V., Zaitseva N. A., Khrapov S. S., 2021, Astronomy Reports, 65, 1215

Zeng G., Wang L., Gao L., Yang H., 2024, MNRAS, 532, 2558

Zhang L., Zhu L., Pillepich A., Du M., Jiang F., Falcón-Barroso J., 2025, A&A, 699, A320

Zinger E., et al., 2020, MNRAS, 499, 768

van de Voort F., Bahé Y. M., Bower R. G., Correa C. A., Crain R. A., Schaye J., Theuns T., 2017, MNRAS, 466, 3460

van den Bosch F. C., Jiang F., Campbell D., Behroozi P., 2016, MNRAS, 455, 158

van der Wel A., Bell E. F., Holden B. P., Skibba R. A., Rix H.-W., 2010, ApJ, 714, 1779